



**STScI** | SPACE TELESCOPE  
SCIENCE INSTITUTE

## Instrument Science Report WFC3 2016-05

# UVIS 2.0: Ultraviolet Flats

J. Mack

March 06, 2017

---

### ABSTRACT

*Improved UV flat fields were delivered on February 23, 2016 for the four bluest WFC3 filters. These new reference files correct for sensitivity residuals in a crosshatch pattern on spatial scales of  $\sim 50$ -100 pixels. The residuals are a result of in-flight temperature differences affecting the detector's spatial response, which was derived from ground test data at a warmer operating temperature. Photometry of white dwarf standards stepped across the UVIS detector shows a linear correlation between the flat field response and the measured flux residual, which is used to model the correction. With the 2016 flats, the photometric repeatability is now 3.0% peak-to-peak (0.7% rms) compared to 6.7% peak-to-peak (1.8% rms) with the original 2011 flats, excluding the left edge of the detector ( $x < 300$  pixels) in F275W where photometry is  $\sim 1\%$  higher than the rest of the frame. The UV filters have color terms of several percent, and the new chip-dependent calibration is intended to produce uniform count rate across the two chips for blue sources. When using the inverse sensitivity values delivered in February 2016, offsets in the UV count rate between chips of up to 2% are found for hot stars, and even more for cool stars. A revised calibration delivered in November 2016 corrects the offset for blue sources, allowing for more accurate drizzled data products when combining pixels from different UVIS chips.*

---

### I. Introduction

Flat fields for WFC3's UV filters were obtained during thermal vacuum ground testing in 2008. In order to obtain sufficient signal in the UV filters F218W, F225W, F275W and F280N, the flats were obtained with the deuterium lamp at a warmer temperature ( $-49^\circ\text{C}$ ), than the nominal operating temperature ( $-82^\circ\text{C}$ ) in order to achieve higher count rates. Differences in the UV spatial response with temperature were expected, with in-flight calibration observations planned to correct for this effect. With a total signal  $> 75,000$  electrons per filter, the rms error from Poisson counting statistics is  $< 0.4\%$  per pixel (Sabbi et al. 2009). These flats map the pixel-to-pixel response of the detector and are referred to as P-flats in this report.

For the bluest UVIS filters, spatial structure at scales of  $\sim 50$ -100 pixels is visible in the flats. This structure is notably stronger in UVIS1 (top chip) compared to UVIS2 and almost entirely disappears at wavelengths greater than  $\sim 500$  nm. This was originally referred to as a ‘crosshatch’ pattern by Baggett (2007) and as a ‘quilt’ pattern by Sabbi (2008). At ultraviolet wavelengths, the UVIS2 detector achieves higher sensitivity than UVIS1, and the sensitivity difference increases toward shorter wavelengths (Brown 2008). Sabbi et al. (2009) note a displacement in the peaks of the flat field histogram for each chip and attribute at least half of the offset to inherent throughput differences between chips and the other half to temperature effects. When creating the 2009 flat field reference files (t\*pfl.fits), the UVIS2 chip was normalized to UVIS1 so that any sensitivity differences between chips were corrected by CALWF3 during the flat field correction FLATCORR. Consistent with the ACS/WFC approach, this meant that a single zeropoint value could be applied to both chips.

Improved flats were delivered to MAST in December 2011, which correct for a large internal reflection or ‘flare’ in the ground flats and for in-flight differences in the detector response computed from dithered photometry of Omega-Cen (Mack et al. 2013). Star cluster data were obtained for only the most popular broadband filters, so the same low-frequency (L-flat) corrections for F225W and F275W were used to correct the F218W and F280N filters, respectively. Due to the limited spatial density of bright stars in the UV, the L-flat solutions were computed by dividing the detector into a 16x16 grid (with each grid point representing 256x256 detector pixels) and then solving for independent values at each grid position. This ‘pixelized’ L-flat for each filter was then smoothed and multiplied by the original (ground) P-flat to produce the 2011 LP-flat reference files (v\*pfl.fits).

To verify the accuracy of the improved 2011 flats, white dwarf (WD) standards were stepped across the UVIS detector to measure the spatial repeatability of the photometry. In the first set of observations, Mack et al. (2015) noted that when the star was placed on low (high) sensitivity regions of the crosshatch in F275W, the measured flux was fainter (brighter) than expected. Additional calibration observations were obtained for the remaining three UV filters in an effort to model any temperature-dependent residuals correlated with the crosshatch.

In February 2016, the WFC3 team moved to a chip-dependent approach to the UVIS photometric calibration, referred to as UVIS 2.0. In the new approach, the L-flats have been recomputed using CTE-corrected star cluster data and then normalized to the median value of each chip (Mack et al. 2016). To ensure that photometry in calibrated (\*flt.fits) images remains continuous across the two chips, the improved CALWF3 (version 3.3) contains a new step (FLUXCORR) that scales the UVIS2 science pixels by the chip sensitivity ratio so that users still only need to keep track of a single set of zeropoints. The chip ratio is now based on photometry of WD standards measured separately on UVIS1 and UVIS2 (Deustua et al. 2016). As a result, WFC3 photometry is significantly improved for UV observations of blue sources, since the sensitivity ratio is now determined from WD standards rather than the redder average cluster population. Calibrated data products are further improved for the F218W and F280N filters, where the chip ratios were based on L-flats from F225W and F275W, respectively, but are now computed from direct WD observations on both chips for every UVIS filter.

Mack et al. (2016) describe the improved chip-dependent flats for 42 UVIS filters (z\*pfl.fits) delivered in February 2016 but defer the details of the UV temperature correction to this ISR. Section 2 describes initial testing with the F336W ground flats obtained at both -49C and -82C. The ratio of these two sets of flats correlates directly with the crosshatch pattern and suggests that similar spatial residuals may still be present in the UV flats. Section 3 provides more detail on the stepped WD calibration data, and Section 4 compares the derived temperature-correction model with the F336W data. Section 5 quantifies the improvement in the photometric repeatability with the original 2009 flats, compared with the 2011 and 2016 solutions. Color terms in two UV filters are explored in Section 6 by splitting Omega-Cen into separate populations and measuring differences in count rate for the same stars on different chips. Section 7 summarizes the results of this study and highlights work in progress to further improve the accuracy of UV photometry. In recognition of the unique UV capabilities of HST and the finite lifetime of the mission, the ‘UV Initiative’ introduced in Cycle 21 continues into Cycle 25 (Strolger & Rose 2017), so this improved photometric calibration is critical in supporting that effort.

## II. F336W Ground flats

Among the ground test data obtained in 2008 are flat fields at both -82C and -49C using the xenon lamp in F336W (Sabbie et al. 2009). Understanding how the detector temperature impacts the spatial response for F336W may give some insight into how to correct the UV flats, which were obtained only at -49C. The ratio of the two sets of F336W flats is presented in the right panel of Figure 1, which shows a residual crosshatch pattern of  $\pm 3\%$  peak-to-peak. A similar residual pattern may be required to correct the UV flats to the -82C in-flight temperature.

The sensitivity of the WFC3/UVIS detector in the 2000-3500 Å range is achieved by the adoption of aluminum mirrors with magnesium fluoride ( $\text{MgF}_2$ ) coatings in the optical train. (Giavalisco et al. 2002). Figure 2 compares the UVIS1 and UVIS2 throughput at the blue end of the spectrum. Overplotted in color are the UV filter throughput curves from SYNPHOT (Brown 2006) along with the F336W bandpass for comparison. Noting the dip in throughput at  $\sim 2800$  Å, caution is used in assuming that the F336W temperature-sensitivity ratio will be directly applicable to the bluer UV filters. Similarly, since the F336W flats were created using the xenon lamp, the temperature-sensitivity relation may differ for the UV flats which were created using the deuterium lamp.

Histograms of the F336W flats are shown in Figure 3, with the -82C flats in black and the -49C flats in red. Differences in the flat quantum efficiency (QE) with temperature are more pronounced for UVIS1 compared to UVIS2. The broad tail of low sensitivity pixels in UVIS1 reflects the stronger crosshatch pattern seen in the flats for that chip. This low sensitivity tail is notably stronger in the -82C flat compared to the -49C flat. The dip in the UVIS2 flat histogram at  $\text{QE} \sim 1$  is due to a small gain offset between amps C and D, which can be seen in the left panel of Figure 1. This offset is not apparent in either the flat ratio image (-82C/-49C) shown in Figure 1 (right) or in the histogram of the flat ratio shown in Figure 4, suggesting that the CCD gain is relatively insensitive to temperature effects.

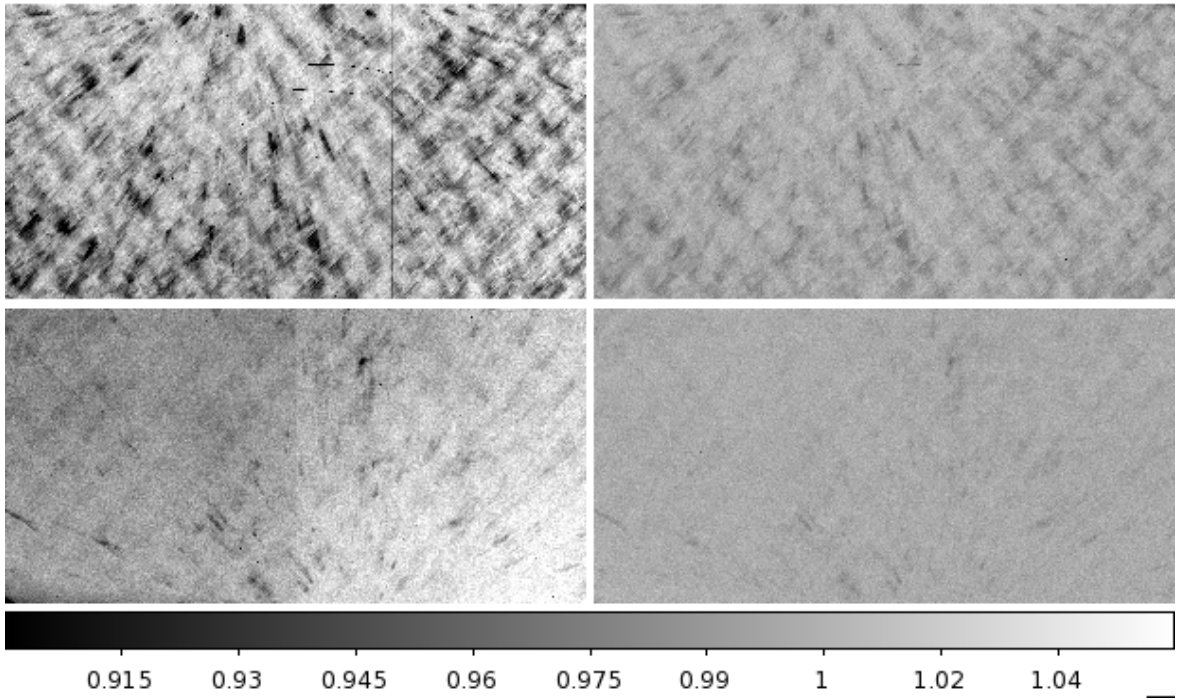


**Figure 1:** The F336W ground flat acquired at -82C (left), where black indicates pixels with lower sensitivity. The ratio of the F336W flats at -82C and -49C (right) shows a residual pattern correlated with the flat field crosshatch. The color bar for the -82C flat and the ratio -82/-49C are both displayed with a total range of 15% (0.90 to 1.05).

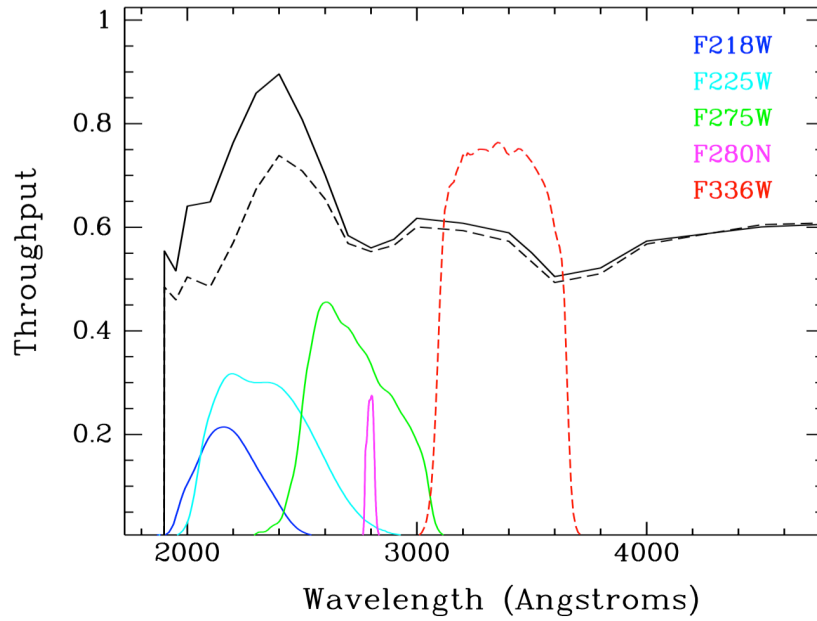


**Figure 2:** Throughput of the UVIS1 and UVIS2 detectors (black: dashed and solid) overplotted with the UV filter throughput. For comparison, the F336W filter is shown as dashed red.



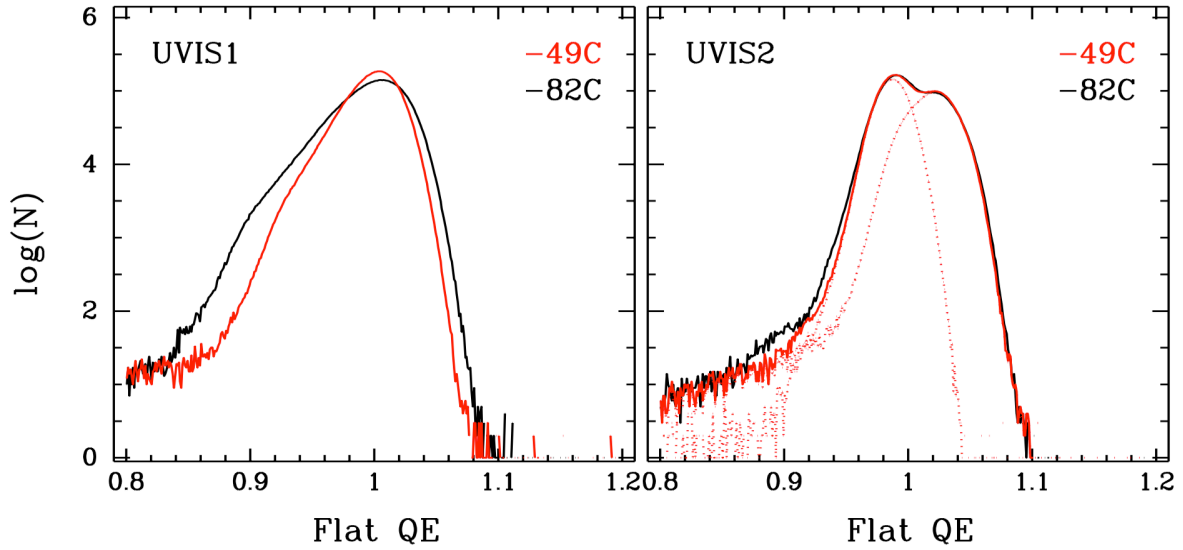


**Figure 3:** F336W flat histograms for UVIS1 (left) and UVIS2 (right), with the -82C flats shown in black and the -49C flats in red. The extended tail of low sensitivity pixels in UVIS1 reflects the stronger crosshatch for that chip compared to UVIS2. The -82C histograms are broader at -82C compared to -49C flats, and the effect is much larger for UVIS1. The central dip in the UVIS2 histograms is due to a gain offset between amps in the flats. Histograms for the C and D amps for the -49C flat are overplotted with dotted lines.

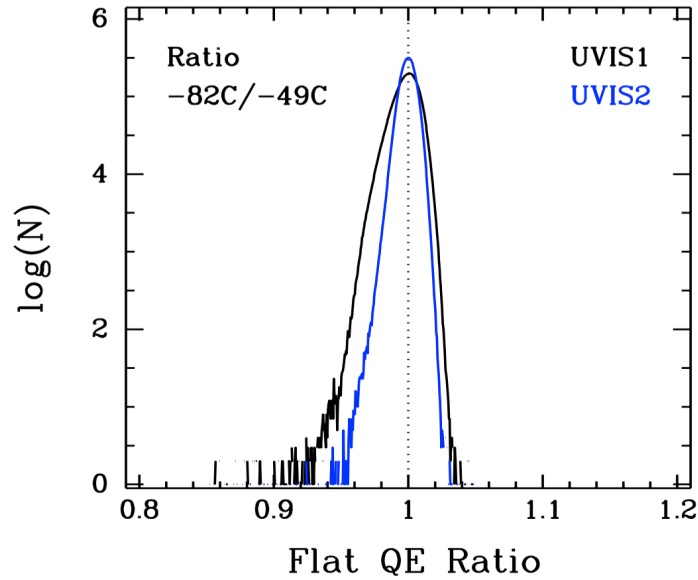


**Figure 4:** Histograms of the F336W flat ratio (-82C/-49C) for UVIS1 (black) and UVIS2 (blue). Sensitivity residuals with temperature are larger in UVIS1 compared to UVIS2. The dip between amps C and D is notably absent in the ratio for UVIS2 suggesting that the CCD gain may be insensitive to temperature effects.

Regions of low sensitivity in flat correlate with low values in the flat temperature-ratio (and vice-versa), and we explore whether there may a simple relation between the two quantities. To do so, the flats were first binned using a 15x15 block average and the flat QE ratio plotted as a function of the -49C flat value. Figure 5 shows that for UVIS1, the majority of points follow a simple linear relation, which is given in Table 1.

In this plot, two populations of points are found with similar slopes but offset by  $\sim 0.005$  or 0.5% in the ratio. The lower population, shown in red, was selected from the graph and overplotted directly onto an image of the flat field. Figure 6 shows that this population corresponds primarily to the right side of the detector ( $x > 3000$  pixels) and suggests that temperature differences produce both mid-frequency (crosshatch) and low-frequency (right side) residuals in sensitivity. Therefore, using a simple linear model to correct for the crosshatch may require an additional L-flat correction to ensure that the measured count rate of a given source is the same over the entire detector. Noting the two populations of points in Figure 5, separate linear fits were computed for the left and right sides of the detector. Table 1 shows that the slope of each fit is the same to within the errors, with only a small shift in the y-intercept.

As an exercise, this linear fit was used to compute a correction image to be applied to the measured -49C ground flat, e.g.  $QE\_ratio(model) = 0.390 * (-49C\_flat) + 0.611$ . Then, the true QE ratio -82C/-49C may be compared to the model QE ratio to get an idea of how well a simple linear correction works. The ultimate goal is to correct for mid-frequency crosshatch residuals ( $\sim 50$ -100 pixels) which are not resolved by the 16x16 L-flat grid, while at the same time preserving the high signal-to-noise pixel-to-pixel structure. Thus, any ‘sharp’ features in the flat, where the QE changes rapidly on scales of a few pixels, were masked before smoothing the correction image. These features are typically detector artifacts which do not appear to follow the linear trend in Figure 5.

To mask these sharp features before computing a correction model, the absolute derivative of the -49C flat was computed using the PyRAF task ‘deriv’. This task calculates the difference of a given pixel with respect to each of its 4 neighbors and saves the largest absolute value of the difference. Next, any pixels with a derivative value  $> 0.05$  were masked in the flat. This cutoff value was determined empirically from inspecting features in the flat and corresponds to  $< 1\%$  of the UVIS detector pixels. Figure 7 shows an example of pixels which were masked before computing the model correction. These include scratches on the UVIS detector and compact groups of low response pixels. Gunning et al. (2014) show that in the UV, low sensitivity pixels typically exist in small groups with sizes of a few pixels. This population evolves with time, and a fraction of these appear to recover following an anneal when the detector is warmed to  $\sim 20C$ . Since this population of anomalous pixels changes with time, they were not included when computing the model correction.

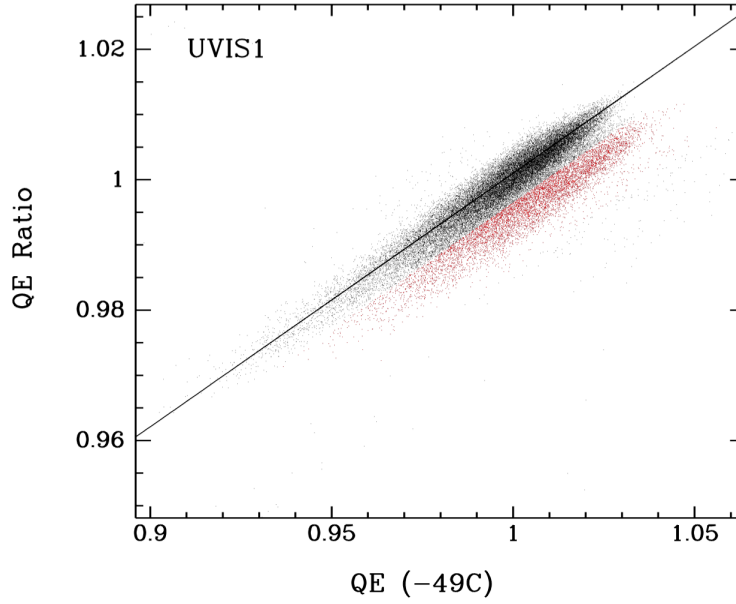


**Figure 5:** F336W flat ‘QE’ ratio (-82C/-49C) versus the flat QE at -49C for the UVIS1 detector. Two populations of points are visible (black vs. red) with similar slope but with the y-intercept offset by  $\sim 0.005$  (0.5%). The solid line reflects a linear fit to the left side ( $x < 3000$  pixels) of the detector only.

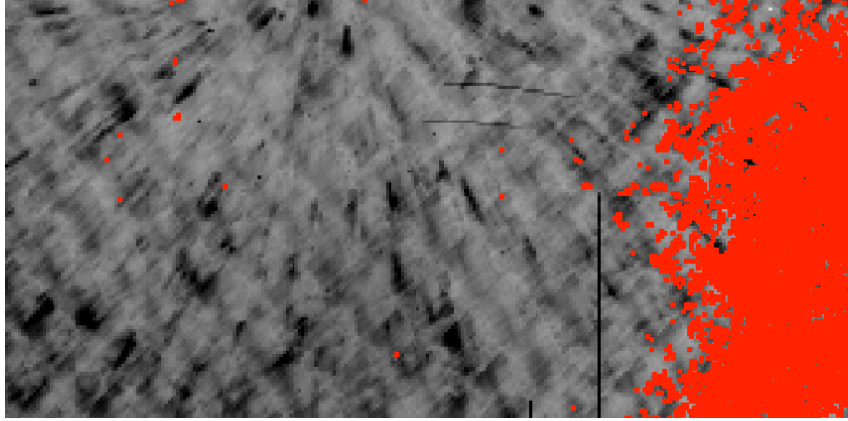


**Figure 6:** The UVIS1 flat field overplotted with the red population of points from Figure 5.

**Table 1.** Linear fits to the points in Figure 5 for the full detector and for the left ( $x < 3000$  pixels) and right ( $x > 3000$  pixels) sides of the detector separately. The last column reflects the number of data points included in each fit from the 16x16 block averaged images, excluding the extreme edges of the detector.

Fit	Slope	Intercept	Chi2	RMS	Npoints
F336W, chip1	$0.380 \pm 0.002$	$0.620 \pm 0.002$	$8.77e-6$	0.0030	28306
F336W, chip1, left	$0.390 \pm 0.001$	$0.611 \pm 0.001$	$3.23e-6$	0.0018	21718
F336W, chip1, right	$0.389 \pm 0.003$	$0.607 \pm 0.003$	$5.62e-6$	0.0024	6695

The -49C flat was then smoothed using an 11x11 median filter, where pixel values less than 0.8 or greater than 1.1 (assumed to be artifacts) were rejected prior to smoothing. The linear fit from Table 1 (excluding the right edge) was applied to the -49C flat to create a model correction image. Finally, the ratio of the model correction with respect to the true flat ratio (-82C/-49C) provides an estimate of the accuracy of the model. Figure 8 (left panel) shows the true flat ratio (i.e. the sensitivity residual) in the left panel and the ratio of the model correction to the ‘true’ correction in the right panel, displayed with the same range. The ratio (model/true) shows a faint residual ‘bowtie’ feature, but nearly all signature of the crosshatch pattern has been removed.

Comparing histograms of the left and right panels from Figure 8, the residual rms is reduced by ~60%. The rms width of the model/true correction (right panel) is ~0.005 or 0.5%, where 95% of pixels are within  $\pm 1\%$  and 99.5% are within  $\pm 1.5\%$ . Gunning et al. (2014) describe an anomalous, evolving population of low sensitivity pixels in the UVIS detector which change with time since the previous anneal. For example, in F225W the total number of pixels deviating by more than 2-3% from the median baseline ranges from 3-10% with time, so outliers in the model/true ratio are expected.

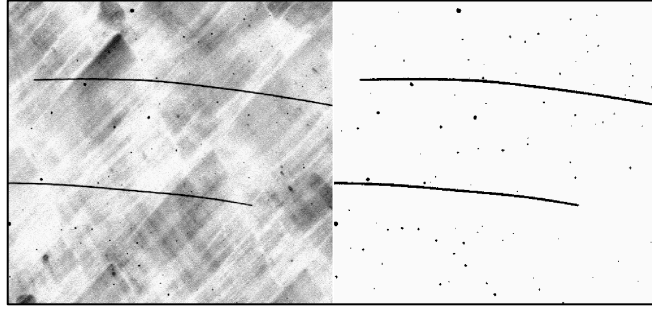


**Figure 7:** A 500x500 pixel region of the F336W UVIS1 flat (left) and the corresponding region of the mask (right). These features do not follow the expected linear relation and were therefore excluded prior to computing a smoothed model correction for temperature.

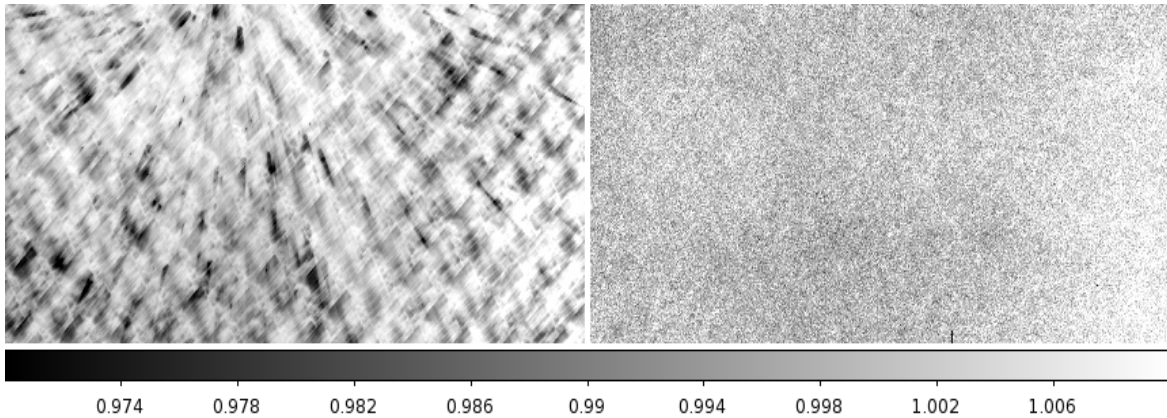


**Figure 8:** The -82/-49C ‘true’ UVIS1 flat residual (left) and the ratio of the ‘model’ to the ‘true’ correction (right). Both panels are displayed with a total range of 4% (0.97 to 1.01). The ratio (model/true) has a mean value of  $1.000 \pm 0.005$  for the detector region  $x < 3000$  pixels. For  $x > 3000$  pixels, the ratio is slightly larger at  $1.006 \pm 0.005$ . A faint residual bowtie can be seen in the ratio and was reported by Sabbi et al. (2009) as a feature in the ground flats.

Next, we investigate whether a similar linear relation applies to the UVIS2 detector. As in Figure 5, the flat temperature ratio (-82/-49C) is plotted versus the flat -49C QE value in Figure 9. The black points show that the total range of the ratio is much smaller than for UVIS1, but with no strong linear trend. Noting that the flat ratio in Figure 1 is continuous across the two amplifiers, the gain offset was removed from the -49C flat, and the ratio is overplotted as the points in red. This tightens the previous distribution but still shows no obvious trend. In Figure 10, the UVIS2 flat is shown in panel A and the flat with the gain offset removed in panel B. Noting a diagonal gradient in panel B which looks similar in shape and scale as the UVIS2 pixel area map (PAM), the flat was then divided by the PAM in panel C. This may be compared to the ‘true’ -82/-49C flat ratio in panel D. Because these two panels look remarkably similar, the values from panel C were overplotted in Figure 9. These are shown green points which fall primarily under the blue points, with the exception of a small population of pixels with larger QE).

Excluding the right edge of the detector ( $x > 3000$  pixels), the points are overplotted in Figure 9, this time in blue. Superimposed on the graph is the linear fit from Table 1 for the right side of the UVIS1 detector, which matches the slope of the blue points remarkably well. Since the crosshatch is less prevalent in UVIS2 flats, that explains why the flat ratio histogram in Figure 4 is narrower compared to UVIS1 and also why the distribution of points along the y-axis in Figure 9 covers a much smaller range.

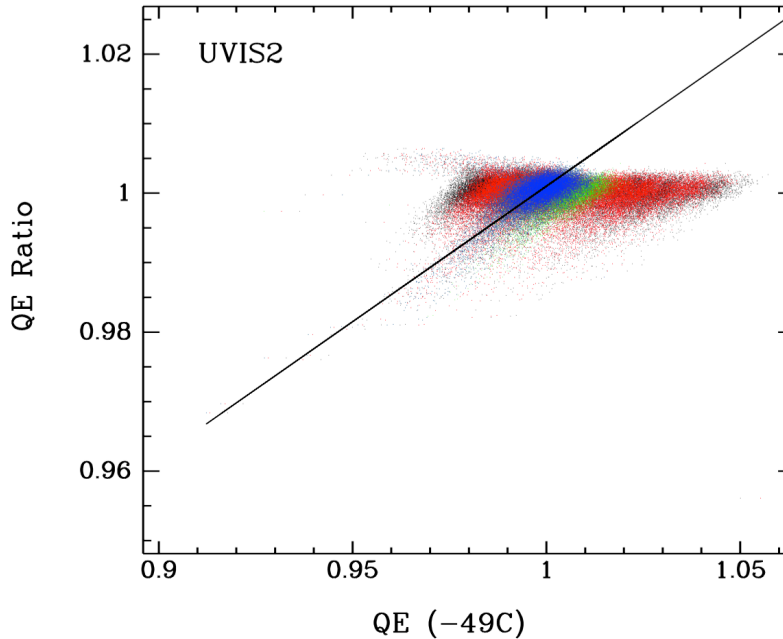


**Figure 9:** The F336W flat ratio (-82C/-49C) vs. flat QE (-49C) for UVIS2 (black). Red points show a flat which has been normalized to remove the gain offset between amps. Green points have had an additional correction to divide by the pixel area map. Blue points are the same as green but exclude the right edge of the detector. The UVIS1 linear fit from Figure 5 is overplotted and does a good job matching the blue points.

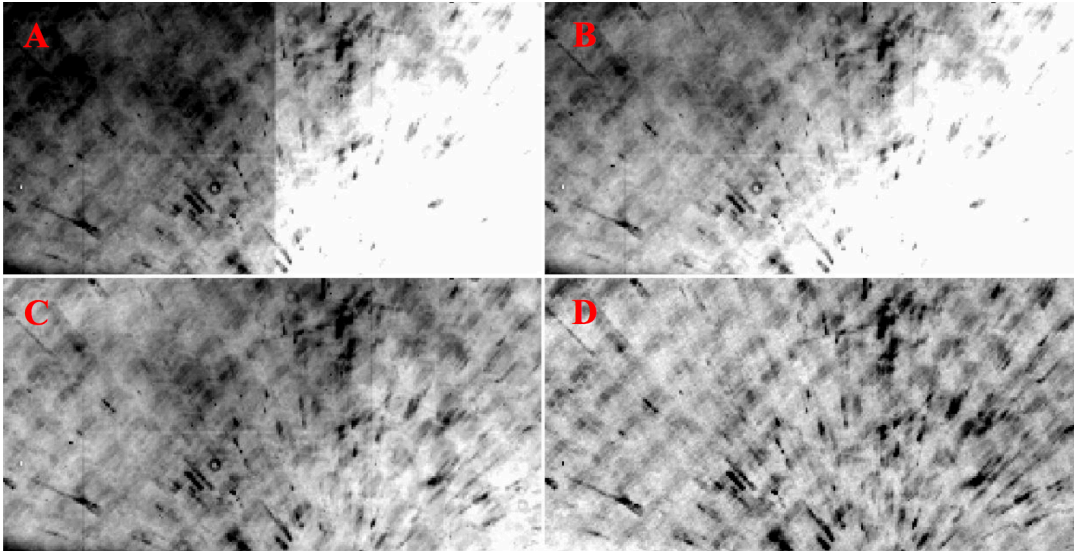


**Figure 10:** (A) The UVIS2 flat field, (B) with the amplifier gain offset removed, (C) divided by the PAM, and (D) compared to the ‘true’ -82/-49 flat residual. Panels C and D look remarkably similar after applying the PAM and the gain offset to the flat.

The F336W ground flat ratio tests suggest that the changing the detector temperature results primarily in crosshatch residuals in UVIS1, with a smaller low-frequency component at the right edge of the detector. For UVIS2, the crosshatch residual is much weaker, but it appears follow the same linear relation as for UVIS1 after applying the PAM. The impact of temperature for UVIS2, therefore, appears to be primarily low-frequency residuals that vary across the chip and which are similar in shape and strength as the PAM. Understanding how temperature affects the spatial response in F336W provides some insight into developing a model to correct the UV ground flats.

### III. Stepped Photometry

Because of their lower f-ratio, flat fields created with the internal calibration lamps (f/300) cannot be used to correct science observations (f/31). Any imperfections on the filters such as the UVIS droplets will produce an out of focus image at the detector (Gunning et al. 2014). Instead, calibration observations were designed to step HST WD flux standards across different portions of the UVIS detector to quantify any spatial variability in the photometry. When a source is observed at multiple locations across the detector, its photometric repeatability can provide an estimate of the flat field spatial accuracy. With a signal-to-noise of  $\sim 500$  for each standard, the Poisson-error ( $1/\sqrt{N_{\text{electrons}}}$ )  $\sim 0.2\%$  gives a lower limit to the photometric repeatability.

The stepped UV calibration observations are by described in detail by Mack et al. (2015). To summarize, the first program 12707 stepped the same star across known ‘features’ in the F275W, F438W, F606W, and F814W flats; for example, to verify how well the ‘flare’ in the 2009 ground flats was removed in the 2011 corrected flats. Figure 11 (left panel) shows portions of the detector sampled in this program superposed onto an image of the F275W flat field, where dark regions correspond to lower detector sensitivity. While this initial dataset did not intentionally sample the ‘crosshatch’ pattern apparent in the flats at blue



wavelengths, the largest photometric deviations in F275W were found when the star was placed on these lower sensitivity pixels.

Additional stepped observations for the F218W, F225W, and F280N filters were obtained in the next two calibration cycles, in programs 13096 and 13584. This time, detector positions were carefully selected to place the star on pixels with reduced sensitivity in the flat and also on adjacent regions with higher sensitivity. A similar number of both low and high sensitivity regions were sampled to determine whether the observed crosshatch residuals could be fit using a simple linear model, as done for the F336W filter. The detector positions sampled in the later two calibration programs are shown in Figure 11 (right panel) superposed onto an image of the F225W flat field.

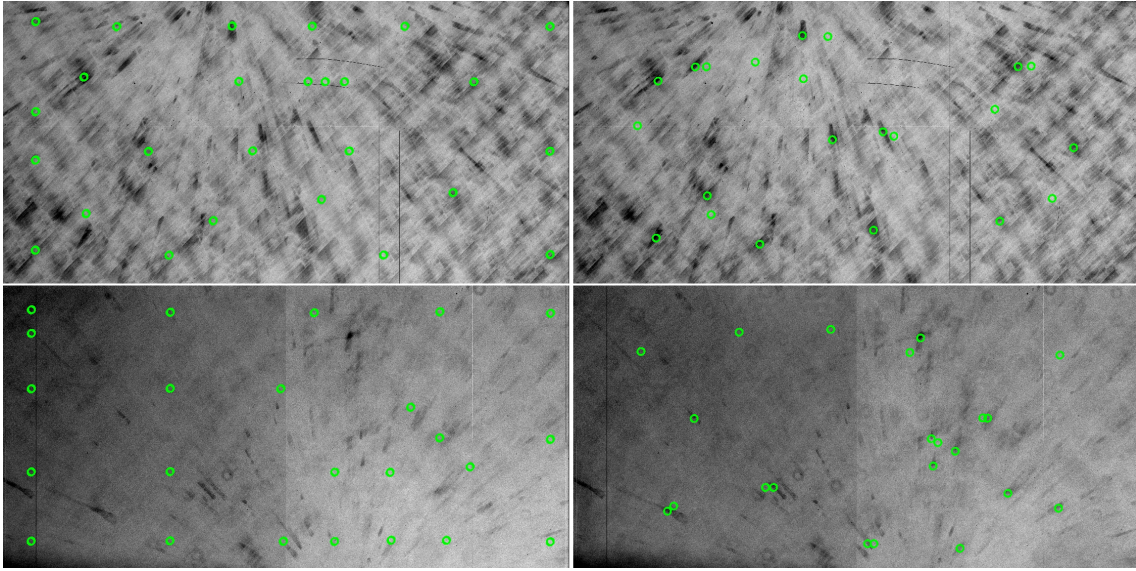


**Figure 11:** (Left) Stepped positions for F275W superposed on an image of the flat field. (Right) Stepped positions for F218W, F225W, & F280N superposed onto an image of the F225W flat field. For the later program, care was taken to place the star on low (dark) and high (light) sensitivity regions of the UV crosshatch pattern.

As described by Mack et al. (2015), photometry was measured in a 10-pixel aperture and the sky background computed from the mode in an annulus between 75-125 pixels. Because the star was measured twice at each detector position, dithered by only a few pixels, the average of the two measurements was computed for each position. Photometry was derived from both drizzled frames and from calibrated (\*flt.fits) frames corrected for distortion using the PAM. The two approaches produce similar spatial residuals to within 0.1%.

For each filter, the mean flux was computed for each chip, and the fractional residual relative to the mean for each subarray position was then mapped to full-frame detector coordinates. Figure 12 shows the F218W spatial repeatability for observations calibrated with the 2009 ground flat at -49C (top) and with the 2011 in-flight flat (bottom) which includes a low-frequency correction based on dithered Omega-Cen data. While the 2011 flats improve the overall spatial residuals, especially for UVIS2, they do not correct large deviations due to the crosshatch structure. Flux residual maps for all four UV filters using the 2011 flats are shown in the top panels of Figures 21-24 at the end of this report.



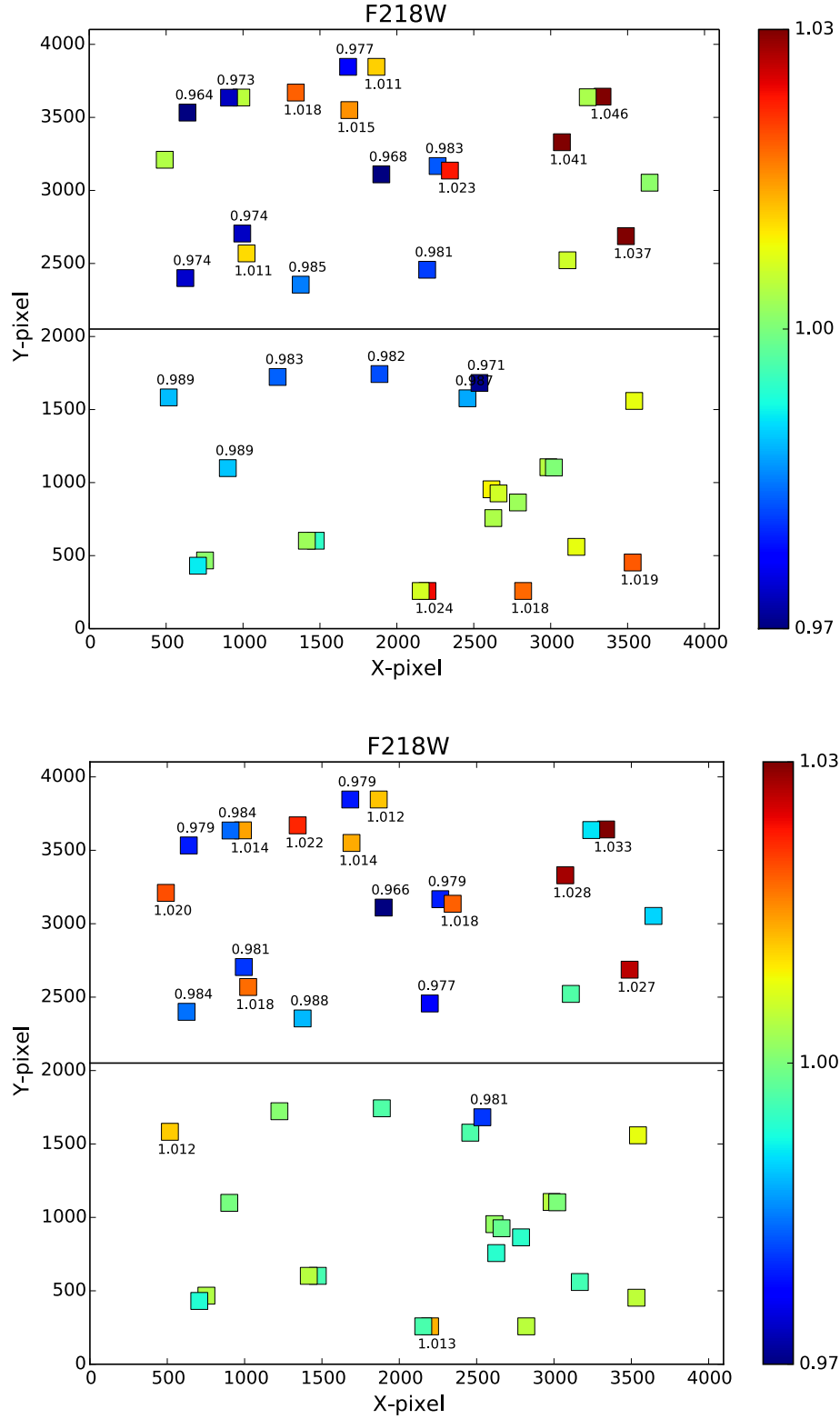


**Figure 12: Fractional residual relative to the mean flux per chip for G191B2B observed in F218W, calibrated with the 2009 ground flats (top) and the 2011 flats (bottom), which include a low-frequency correction derived from in-flight data.**

As discussed in Section 2, the temperature residual for UVIS2 in F336W follows the UVIS1 linear relation after applying a smooth correction resembling the PAM. Flats delivered in 2011 for the UV filters already contain a low-frequency correction based on in-flight data. For example, the F275W L-flat correction from 2011 is shown in Figure 13 (left) along with a comparison of the PAM (center) and the L-flat/PAM (right). For UVIS2, the right panel is relatively flat, except for the right side of the detector which is  $\sim 1\%$  lower than the rest of the frame. This agrees qualitatively with the F336W tests which suggest that a change in temperature creates not only a crosshatch residual but also a low-frequency component at the right edge of the detector. Flux residuals in Figure 12 show that the smooth gradient across UVIS2 when using the 2009 flats is primarily removed with the 2011 flats after applying the L-flat. Thus, the effect of temperature for UVIS1 appears to be a strong crosshatch residual and weaker L-flat component, while the effect for UVIS2 is primarily an L-flat with a weaker crosshatch component.

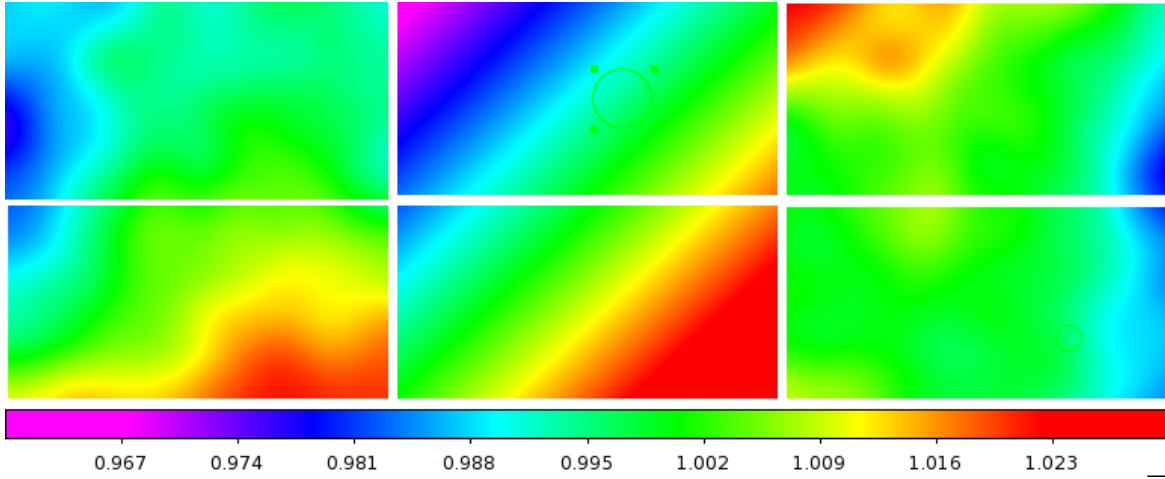


**Figure 13:** (Left) The F275W L-flat correction derived using Omega-Cen, with UVIS1 on top and UVIS2 on bottom. (Middle) The UVIS pixel area map displayed with the same total range as the L-flat. (Right) The ratio (L-flat/PAM) is relatively flat for UVIS2 except for the right edge, which is up to 1% lower than for the rest of the chip.

#### IV. UV Model

Comparing the spatial residuals in Figure 12 with their position on the flat from Figure 11, we find that a star's observed count rate is lower when it falls on a darker region of the crosshatch, corresponding to lower detector sensitivity. For example at  $(x=1683, y=3846)$ , the dark feature in the 2011 UVIS1 flat produces photometry which is 2.1% fainter than the mean, but for an adjacent bright region at  $(x=1867, y=3846)$  produces photometry which is 1.2% brighter than the mean. This is consistent with the F336W prediction that the flat field value correlates directly with the temperature-sensitivity residual (Figure 5).

Following this logic, the measured flux residual for all stepped UV observations is plotted in Figure 14 versus the 2011 flat value, where each chip has been normalized to a value of 1.0. Since the sensitivity residual for F336W shows no discontinuity between amps C and D (e.g. Figures 1 and 4), the gain offset was removed from the UVIS2 flat value prior to plotting. This changes the UVIS2 flat histogram in Figure 3 from a bi-modal to a single Gaussian distribution.

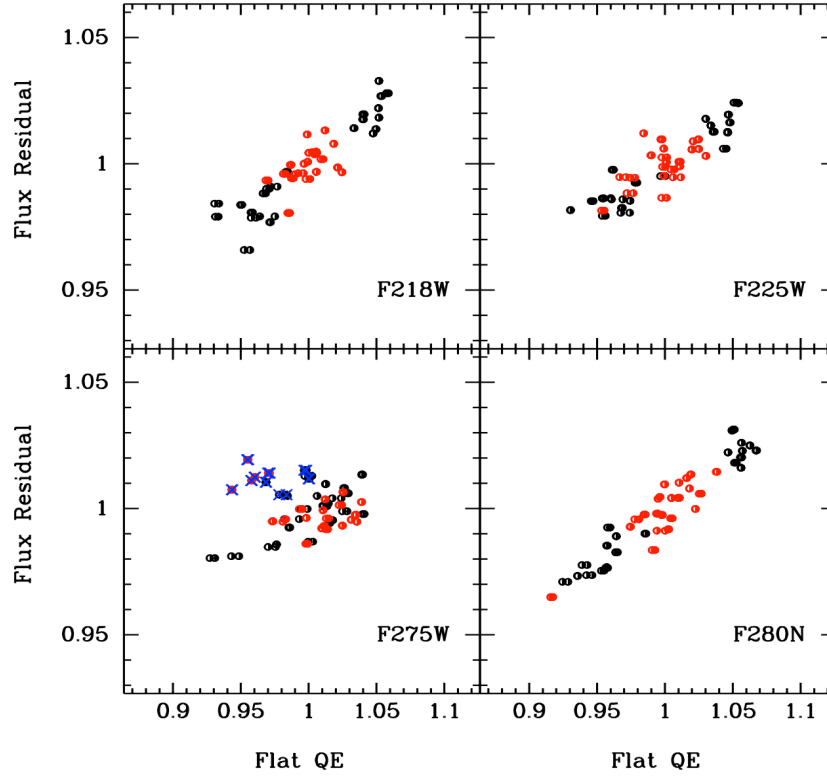


**Figure 14:** Flux residual with respect to the mean per chip for stepped white dwarf photometry versus the 2011 flat field value, where UVIS1 is shown in black and UVIS2 in red. For F275W, subarrays near the far left edge of the detector on both chips are shown as blue crosses and are excluded from the linear fits in Table 2.

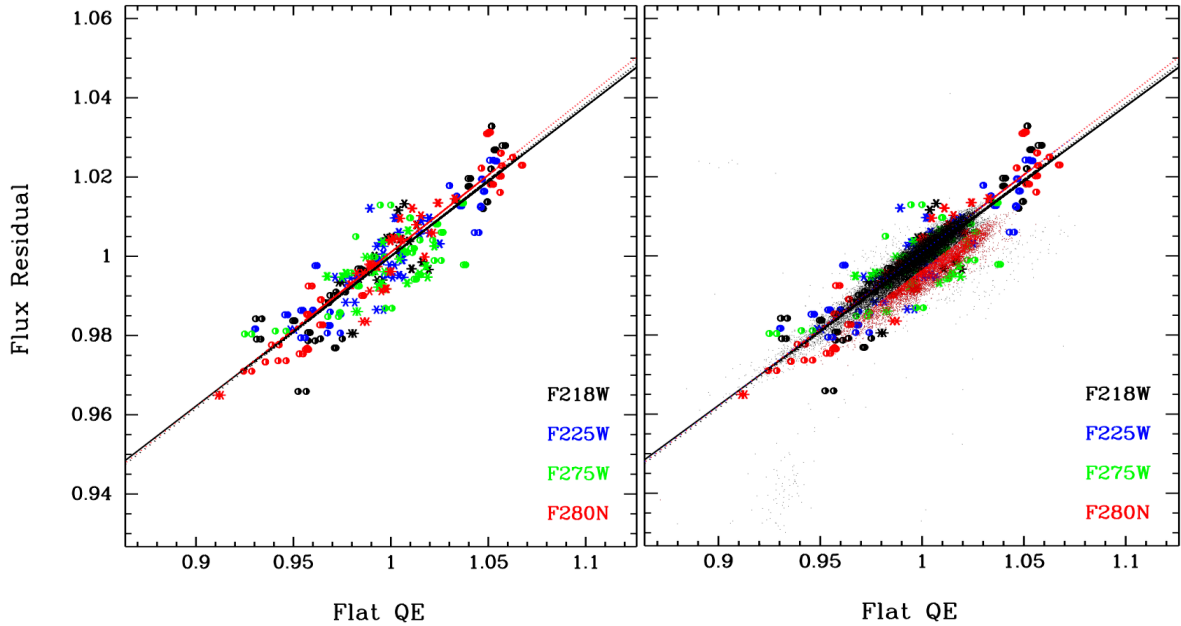


**Figure 15:** (Left) Same as Figure 14, but with all filters overplotted. UVIS1 data is represented with circles and UVIS2 with stars. (Right) Same as left but with the F336W data from Figure 5 overplotted. The best linear fit for all UV stepped data is overplotted as solid black, and the UVIS1-only fit as dotted black. For comparison, the linear fit for F336W UVIS1 is overplotted as dotted red.

Flux residuals from stepped photometry are shown in Figure 14 for UVIS1 black and UVIS2 in red. The x-axis represents the average value of the flat measured in a 10-pixel aperture at the position of the star in the full frame image. Because the F218W, F225W, and F280N observations were specifically designed to sample the crosshatch, a more pronounced linear trend is seen for those three filters compared to F275W. The flux residuals are larger in F218W and F280N (6.7% and 6.6% peak-to-peak) compared to F225W and F275W (4.5% and 3.9% peak-to-peak). This suggests that the crosshatch temperature-sensitivity residual is stronger in these two filters.

A number of outliers (blue crosses) can be seen for F275W. These correspond to subarrays placed at the far left edge of the detector  $x=259$ , shown in the left panel of Figure 11. These points were excluded from linear fits but can be seen in the spatial maps in Figure 23, where the residuals are systematically 1-2% higher than the rest of the detector in the 2011 flat. These particular subarrays overlap the physical overscan region, so the calibrated data products are  $489 \times 512$  instead of the usual  $512 \times 512$ . One possibility is that CALWF3 does not select the proper region of the flat field in these cases. Another explanation is that the L-flat derived for this filter may be inaccurate at the left edge due to an insufficient number of blue stars in Omega-Cen at this position. To test this, the stepped data were recalibrated using the 2009 flats, and these show a mean residual at the left edge of  $0.999 \pm 0.008$  compared to  $1.014 \pm 0.005$  when using the 2011 flats. This supports the hypothesis that the ‘pixelized’ L-flat solution in the UV may be less reliable at the left edge of the detector ( $x < 300$  pixels, or more conservatively  $x < 500$  pixels).

Figure 15 plots the stepped data for all four UV filters onto a single graph. For comparison with Figure 5, the F336W ground test data for UVIS1 are overplotted in the right panel. Lowest flux residual in Figure 15 is for F280N (0.965) at ( $x=2537$ ,  $y=1682$ ) on UVIS2. This corresponds to a small dark feature in the flat (Figure 12) which is  $\sim 50 \times 50$  pixels in size. Since the UVIS2 data were already corrected for low-frequency sensitivity residuals, they fall along the same line as the UVIS1 data.

Linear fits to the data are given in Table 2, where the first four rows give separate fits per filter based on UVIS1 observations only. For the UV filters, the column ‘number of points’ column in Table 2 is twice the number of stepped positions on the detector since each position has two exposures separated by a small line dither. Subarrays for the F218W, F225W, and F280N filters sampled 22 positions (44 exposures) on UVIS1 and 22 positions (44 exposures) on UVIS2. Subarrays for the F275W filter sampled 26 positions on UVIS1 and 24 on UVIS2, but 4 from UVIS1 and 5 from UVIS2 were rejected due to systematically high residuals ( $\sim 1\%$ ) at the far left edge of the detector. These are discussed in more detail in Section 5. This leaves a total of 22 positions on UVIS1 and 19 on UVIS2 in F275W. The total for all UV filters is therefore 88 positions (176 exposures) on UVIS1 and 85 positions (170 exposures) on UVIS2. For the F336W ground flats, the ‘Npoints’ column represents the total number of pixels in the  $15 \times 15$  binned flat, excluding the right edge of the detector.

The next three rows in Table 2 report the fit to all four UV filters simultaneously, including both UVIS chips together and also for chips 1 and 2 separately. Removing the gain offset between amps from the UVIS2 flats prior to fitting reduces the error in the slope and intercept and improves the fit rms and  $\chi^2$  values. The resulting fit has a slightly larger slope and a smaller intercept value, when compared a fit with no gain correction. This result is more consistent with the combined UVIS1 solution for all UV filters and also with the

UVIS1 fit for F336W from Figure 5. The slope and intercept values reported in Table 2 are consistent to one another to within the reported errors.

The best fit to the full set of UV stepped data (four filters, both chips) is plotted as a solid black line in Figure 15. Overplotted is the UVIS1 fit only (dashed) which is nearly indistinguishable from the solid line. For comparison, the best fit to the F336W UVIS1 data (excluding the right edge) is overplotted as a dashed red line. The similarity between the individual fits is remarkable and supports adopting a single linear model to correct all four UV flats based on slope of the combined fit.

Instead of correcting the 2011 flats directly, new chip-dependent flats were computed, as described in Mack et al. (2016). These are nearly identical to the 2011 flats except that the L-flat was computed for each chip separately using CTE-corrected observations of Omega-Cen and then normalized to its median value. These differences amount to a few tenths of a percent, primarily at the edges of the detector, so the linear model from Table 2 should still apply, with the effect of reducing the scatter in the points in Figure 15.

Following the same methodology for F336W, sharp features in the flat were masked and the gain offset removed from chip 2 prior to smoothing with an 11x11 pixel median filter. A separate correction image was computed for each filter by multiplying the combined UV linear fit by the smoothed filter flat. The -49C chip-dependent flats were then multiplied by the temperature-correction image for each filter in order to remove the crosshatch residuals. Finally, each chip was again normalized by its median value.

**Table 2. Linear fits to the flux residual versus flat field QE from Figures 14 and 15. The fit to the F336W temperature-sensitivity flat field residuals is included for comparison. The three fits highlighted in red are overplotted on the data in Figure 15.**

Fit	Slope	Intercept	$\chi^2$	RMS	Npoints
F218W, chip1	$0.391 \pm 0.027$	$0.610 \pm 0.027$	$1.68\text{e-}5$	0.0040	44
F225W, chip1	$0.370 \pm 0.021$	$0.630 \pm 0.021$	$1.94\text{e-}5$	0.0043	44
F275W, chip1	$0.320 \pm 0.049$	$0.678 \pm 0.049$	$1.98\text{e-}5$	0.0043	44
F280N, chip1	$0.406 \pm 0.017$	$0.592 \pm 0.017$	$1.22\text{e-}5$	0.0034	44
UV, chip1	<b><math>0.385 \pm 0.011</math></b>	<b><math>0.615 \pm 0.011</math></b>	<b><math>4.15\text{e-}5</math></b>	<b>0.0064</b>	<b>176</b>
UV, chip2	$0.333 \pm 0.025$	$0.666 \pm 0.025$	$3.25\text{e-}5$	0.0057	170
UV, both chips	<b><math>0.378 \pm 0.010</math></b>	<b><math>0.622 \pm 0.010</math></b>	<b><math>3.72\text{e-}5</math></b>	<b>0.0061</b>	<b>346</b>
F336W, chip1, left	<b><math>0.390 \pm 0.001</math></b>	<b><math>0.611 \pm 0.001</math></b>	<b><math>3.23\text{e-}6</math></b>	<b>0.0018</b>	<b>21718</b>

## V. Results

The same Omega-Cen calibration data used to derive the L-flat may be used to verify the accuracy of the crosshatch correction from stepped WD photometry. As discussed in Section 2, the goal is to determine whether an additional low-frequency correction will be required for the right side of the detector after applying a linear model to correct for temperature. For the two UV filters (F225W, F275W) with dithered observations in program 11911, differential photometry was computed for two exposures oriented 95 degrees from one another.

For these UV filters, Mack et al. (2015) measure color terms of several percent when comparing photometry of the same sources on different chips (e.g. the residual depends on the color of the stars being measured). For this reason, this test has been limited to stars moving across the same chip only (e.g. between amps A and B and between amps C and D). Following the same procedure to derive the 2011 L-flats, aperture photometry was performed in a 5 pixel radius and then corrected to the standard 10 pixel (0.4") aperture using a 9x10 spatial PSF library, which is empirically adjusted to match the mean focus in each image (Bellini & Bedin, 2009; Anderson et al. 2006). More details on the spatial-dependent aperture correction may be found in Mack et al. (2013).

The magnitude difference for matched stars in the rotated set of exposures is plotted versus the detector x-coordinate in Figure 16 for F225W. Residuals in the top panel were computed using the 2011 solution ( $v*pfl.fits$ ) and in the second panel using a flat derived using the new chip-dependent approach (Mack et al. 2016). The rms scatter of differential photometry is noticeably improved when using the CTE-corrected, chip-dependent solution. The third panel plots the residual magnitude when further correcting the flat for crosshatch residuals due to temperature. While the scatter on small spatial scales is lower with the new solution, the average rms over the detector is slightly larger than in panel 2.

For this reason, the full Omega-Cen dataset (27 exposures) was used to solve for a secondary L-flat to correct for low-frequency sensitivity residuals after applying the linear correction model. While the 2011 L-flats for UV filters were computed from a 16x16 grid of independent solutions (Mack et al. 2013), this effect appears to be lower order. The detector was therefore modeled as an 8x8 grid, where each grid point represents 512x512 pixels. Since there is no cluster data for F218W and F280N, the F218W filter was corrected using the F225W L-flat and the F280N using the F275W L-flat. The fourth panel in Figure 16 shows that the rms is further improved with the corrected solutions, and these reflect the set of flat field reference files ( $z*pfl.fits$ ) delivered to the archive in February 2016.

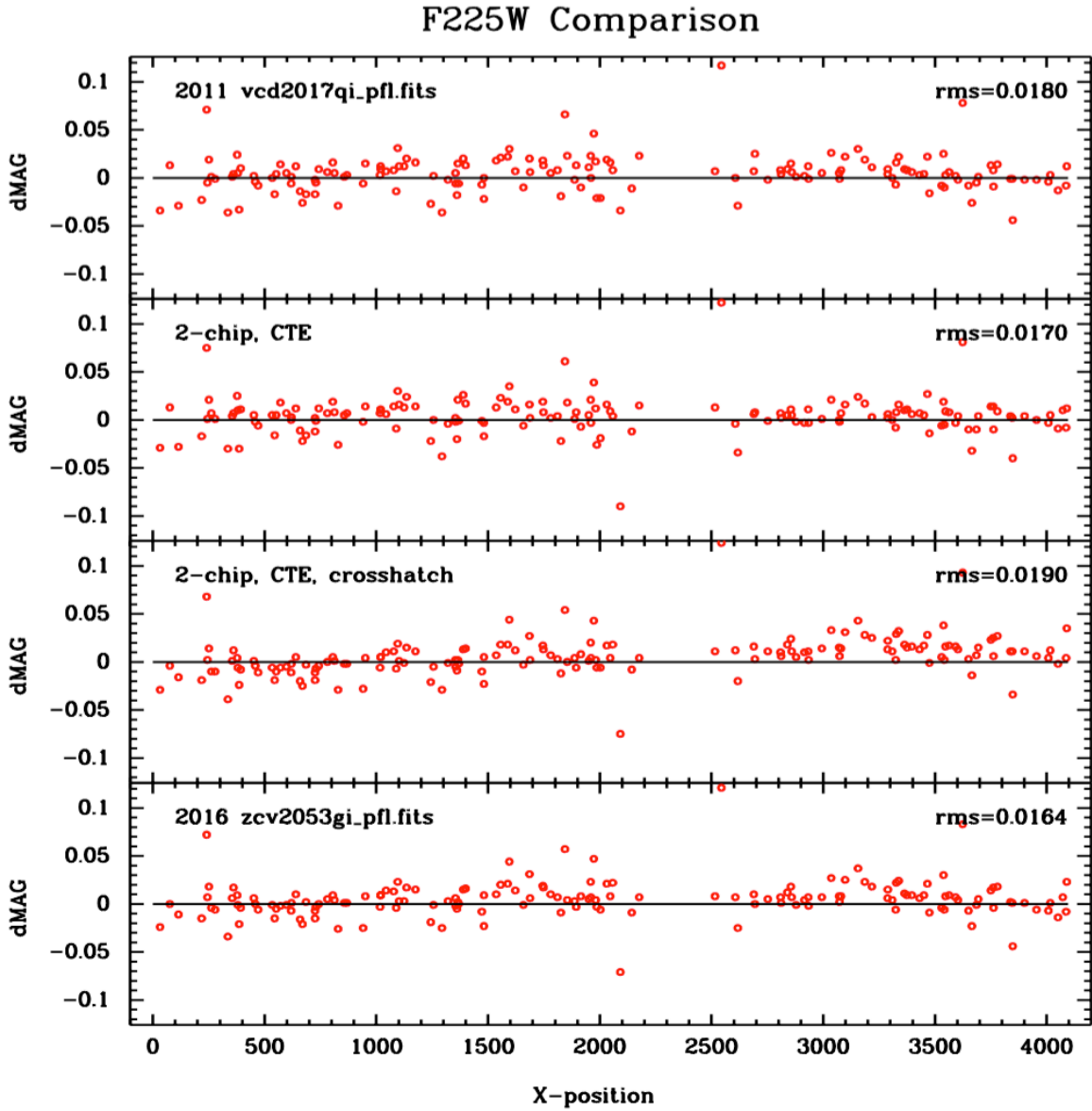


**Figure 16:** F225W delta-mag versus X-position for two Omega-Cen images rotated 95 degrees. Only stars with photometric errors  $< 0.4\%$  are shown. The top panel uses the 2011 flats, the second panel uses the chip-dependent, CTE-corrected flats, and the third panel uses the chip-dependent flats corrected for both CTE and crosshatch residuals. Noting that the points in the third panel do not go through  $\text{dmag}=0$  for  $x > 3000$  pixels, a second low-frequency correction was computed. The bottom panel shows differential photometry with the final 2016 flat field, which gives the smallest rms scatter.



Mack et al. (2016) show that the spatial repeatability of stepped WD photometry is improved significantly with the 2016 UV flats compared with the 2011 solutions. Table 3 reproduces the standard deviation and peak-to-peak range per UV filter from that ISR, but now includes a comparison with the 2009 solutions. These are given as the average over both chips and also for the UVIS1 and UVIS2 chips separately. When using the 2016 flats, the repeatability across both chips is now 3.0% peak-to-peak (0.7% rms) or better compared to 6.7% peak-to-peak (1.8% rms) with the 2011 flats and 8.3% peak-to-peak (2.0% rms) with the 2009 flats. For comparison, the Poisson error per measurement is 0.2% for all four UV filters (e.g. a signal-to-noise  $\sim 500$  for each star).

The spread in the photometry when calibrating with the 3 different sets of flat fields is shown graphically in Figure 17, for UVIS1 (left) and UVIS2 (right). Figure 18 shows the same data but split by year, with the 2011 flats (left) and the 2016 flats (right). The flux residuals may also be visualized as spatial maps of the UVIS detector in Figures 21-24 at the end of this ISR. The color bar in each map spans a total range of  $\pm 3\%$ , and regions of the detector with deviations greater than 1% are annotated on the plots. The top panel of each figure is reproduced from Mack et al. (2015) which quantifies the spatial accuracy of the 2011 flats. The bottom panel shows the improvement with the new 2016 chip-dependent solutions.

From 2009 to 2011, the two chips show roughly equal improvement in the average residual  $\sim 0.5\%$  rms and  $\sim 2\%$  peak-to-peak (P2P) when applying the L-flat. From 2011 to 2016, the most dramatic improvement is seen for UVIS1 where the crosshatch residual is the strongest. This is especially noticeable for the F218W, F225W and F280N filters where the WD standards were carefully positioned on crosshatch features in the flat and where the improvement is as much as 1.9% rms and 4% P2P. For UVIS2, the 2016 flats show a modest improvement for F225W (0.3% rms, 1.4% P2P) and F280N (0.5% rms and 2.6% P2P), whereas the F218W and F275W filters have a similar rms as the 2011 flats and a slightly lower P2P range when excluding the left edge.

For the F275W filter, subarrays were placed in nine positions along the far left edge of the detector ( $x=256$  pixels), as shown in Figure 11. When calibrating these data with the 2009 ground flats, the photometry is within  $0.998 \pm 0.008$  of the mean value. With the 2011 and 2016 flats, however, the photometry is systematically higher at  $1.012 \pm 0.004$  and  $1.013 \pm 0.005$ , respectively. This suggests that the initial L-flat, modeled as a  $16 \times 16$  grid of independent corrections (each covering  $256 \times 256$  native detector pixels) and then smoothed, may be less accurate at the edge of the detector due to the low density of UV-bright stars and fewer measurements at the edges. This also implies that the standard  $512 \times 512$  UVIS subarrays in the left corners of the detector (e.g. *UVIS1-C512A-SUB* and *UVIS1-C512C-SUB*) likely have larger flat field errors than the rest of the detector. Note that this is not the case for similar subarrays placed in six positions along the far right edge of the detector.

Scanned data will be a good check of these solutions, since many more detector pixels are sampled with higher signal-to-noise (e.g. 0.1% photometry). Calibration observations obtained in programs 12713, 13095, and 13583 using a UV-bright double star (Target=GAM-ARI-MIDPOINT, spectral types=A1pSi, B9V) will be useful for validating the accuracy of the improved 2016 UV flats.

**Table 3.** The photometric repeatability per filter as the standard deviation and peak-to-peak (P2P) range of stepped white dwarf observations. The first set of rows reflect the average over both UVIS chips, while the second and third sets of rows give the chip 1 and chip 2 values separately. A second set of F275W values (indicated with an asterisk) excludes subarrays placed at the far left edge of the detector.

Filter	Steps	Stddev (2009)	Stddev (2011)	Stddev (2016)	P2P (2009)	P2P (2011)	P2P (2016)
F218W, avg	44	1.9%	1.5%	0.7%	8.3%	6.7 %	3.0 %
F225W, avg	44	1.6%	1.3%	0.4%	6.8%	4.5 %	1.8 %
F275W, avg	50	1.1%	0.9%	0.8%	5.3%	3.9%	3.5%
F275W*, avg	41*	1.2%	0.8%	0.6%	5.3%	3.3 %	2.7 %
F280N, avg	44	2.0%	1.8%	0.5%	8.2%	6.6 %	2.4 %
F218W, ch1	22	2.4%	2.1%	0.7%	8.3%	6.7%	2.9%
F225W, ch1	22	2.0%	1.6%	0.4%	6.8%	4.5%	1.4%
F275W, ch1	26	1.2%	1.0%	0.7%	5.3%	3.5%	3.1%
F275W*, ch1	22*	1.3%	1.0%	0.6%	5.3%	3.3%	2.7%
F280N, ch1	22	2.6%	2.3%	0.4%	7.9%	6.0%	1.7%
F218W, ch2	22	1.3%	0.7%	0.7%	5.3%	3.3%	3.1%
F225W, ch2	22	1.2%	0.8%	0.5%	4.9%	3.1%	1.7%
F275W, ch2	24	1.0%	0.8%	0.9%	3.7%	3.3%	3.4%
F275W*, ch2	19*	1.0%	0.5%	0.5%	3.7%	2.1%	1.8%
F280N, ch2	22	1.4%	1.1%	0.6%	6.6%	5.0%	2.4%

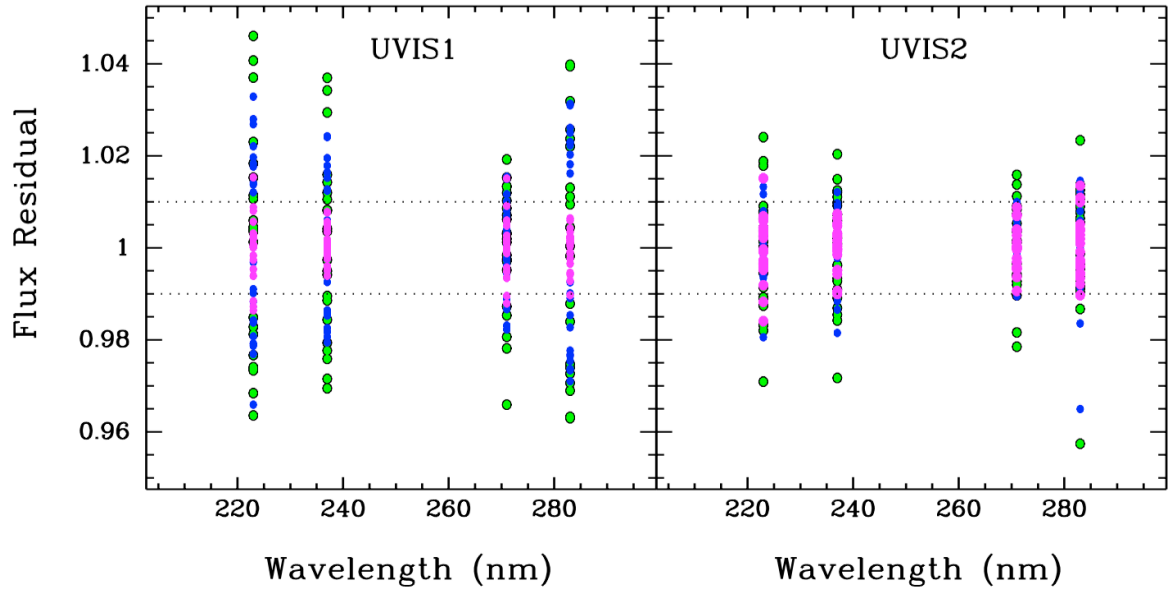


Figure 17: White dwarf flux residual with respect to the mean per chip versus filter pivot wavelength. Data calibrated with the 2009 flats are shown in green, with the 2011 flats in blue, and with the 2016 flats in magenta. The largest deviations are found in UVIS1, which has a stronger crosshatch residual with temperature. For the UVIS2, the 2016 flats show marginal improvement compared to 2011. For the F275W filter, subarrays positioned at the left edge of the detector were excluded from this plot, but are shown in Figure 18.

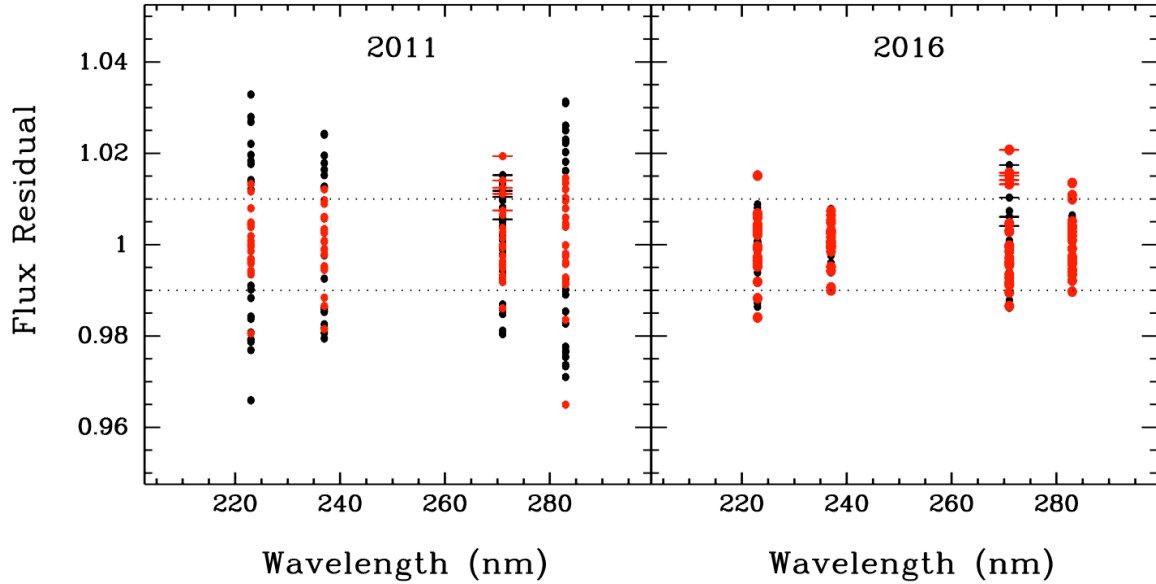


Figure 18: Same as Figure 17, but now comparing the 2011 flats (left) and 2016 flats (right). UVIS1 data is shown in black and UVIS2 in red, as in Figure 14. With the new flats the dashed lines indicate that the majority of points are now within  $\pm 1\%$ . Subarrays placed at the left edge of the detector are indicated with horizontal bars and show  $\sim 1\%$  larger residuals in the 2011 and 2016 flats compared with the 2009 ground flats.

## VI. Color Terms

Bellini et al. (2011) report color effects in the UV calibration observations of Omega-Cen (programs 11452 and 11911) which impact the geometric distortion correction. The authors find a systematic trend in the displacement of the measured coordinates of a star based on its intrinsic color. This is attributed to a chromatic effect induced by the fused-silica CCD windows which refract blue and red photons differently because of a sharp increase in the refractive index below 4000 Angstroms.

Mack et al. (2015) confirm a color effect in the UV filters by showing that relative photometry across the two chips depends on the color of the source. For example, when using L-flats based on dithered Omega-Cen data to define the chip-sensitivity ratio, the stepped WD observations show count rate offsets of  $\sim 5\%$  in F218W and F225W and  $\sim 2.5\%$  in F275W and F280N. This offset is due to the different color of each target, where the average Omega-Cen population used to define the 2011 L-flat is much redder than that of the WD flux standards.

In a second test, the authors select four distinct populations from the Omega-Cen color-magnitude diagram based on their F225W-F275W color. Relative photometry of stars dithered across the two chips shows a constant offset in magnitude that correlates linearly with the color of the source. The measured effect is larger in F225W compared to F275W, and this result is reproduced in the left panel of Figure 19, where only the ‘yellow’ population of stars (F225W-F275W=0.025) has a delta magnitude of 0.0 when calibrated with the 2011 flats.

With the new chip-dependent approach, the flats are normalized to the median value of each chip and therefore longer correct UVIS images for sensitivity differences between the two chips. Instead, the sensitivity ratio is determined from the WD flux calibration observations used to derive the zeropoints (Deustua et al. 2016). With this new approach, the photometry of blue stars should now be continuous across the two chips, with sources redder than the WD’s requiring a color correction. This makes UV photometry non-trivial for sources with multiple populations, particularly old star clusters. In the coming year, the WFC3 photometry team plans to quantify color terms for the UV filters based on synthetic photometry of HST standards of varying spectral type. These enable users to apply the recommended color-correction to the derived zeropoints.

To support the UVIS chip-dependent calibration, CALWF3 (v3.3 and higher) has been revised to make use of the chip sensitivity ratio PHTRATIO (PHTFLAM2/PHTFLAM1) in order to scale the UVIS2 count rate to match UVIS1. Without this scaling, a discontinuity across chips (up to 28% in F218W) would make it difficult to combine images from different chips with AstroDrizzle, which expects the input files to have uniform count rates. This count rate matching is especially important for observations obtained in different epochs (e.g. at varying orientations) or with large dithers such that pixels from different chips are being combined.

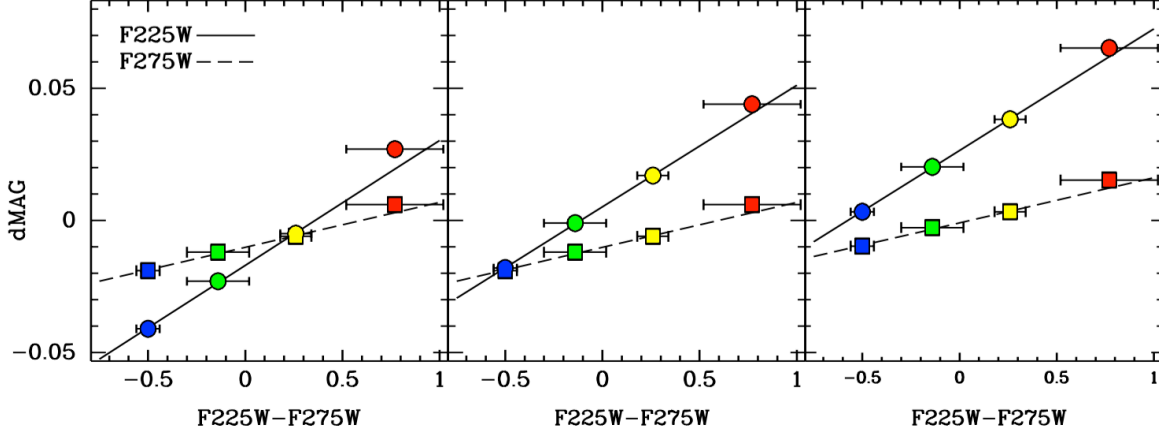


**Figure 19: Magnitude offset versus source color for four populations of stars in Omega-Cen dithered across the chips. Horizontal bars indicate the color range of the subset of objects selected from the CMD. The solid line is a fit to the F225W filter (circles) and the dashed line is a fit to the F275W filter (squares). Red points are likely impacted by the UV red leak so were not included in either fit. The left panel reflects data calibrated with the 2011 flats and zeropoints, and the center panel is based on data calibrated with the chip-dependent solutions from February 2016. The right panel uses a revised image photometry table from November 2016 where the PHTRATIO for UV filters has been adjusted such that the count rate is continuous across both chips for blue sources. For F275W, blue stars still show a small offset from  $d\text{mag}=0.0$ .**

Empirical tests using the new flats and the February 2016 image photometry table (IMPHTTAB= ‘zcv2057li\_imp.fits’) revealed that the PHTRATIO scaling for UV filters F218W, F225W, and F275W did *not* equalize the count rates for blue stars. This is shown in the central panel of Figure 19, where the bluest Omega-Cen population is expected to have a delta-mag of 0.0 with the chip-dependent calibration but which instead shows a residual offset of 0.02 magnitudes ( $\sim 2\%$ ) for both F225W and F275W.

A similar test using the stepped WD data showed that UVIS2 photometry (in electrons/second) is still  $\sim 2\%$  brighter on average than UVIS1 in F225W and F275W and  $\sim 1\%$  brighter in F218W. This is reported in Table 4, where column 4 gives the mean count rate ratio between chips measured in an aperture radius of  $0.4''$  (10 pixels).

Deustua et al. (2017) attribute this count rate offset to differences in the filter response functions for the two chips. In November 2016, the team revised the UVIS2 scaling by a factor reflecting the empirical count ratio of three primary WD flux standards. When recalibrating the stepped WD photometry with the new solution (IMPHTTAB= ‘0bi2206ti\_imp.fits’), the count rate ratio reported in column 5 is now much closer to 1.0 for all filters, except for F275W which is still  $\sim 1\%$  different (but with a similar sized error). For reference, columns 2 and 3 report the PHTRATIO values for the two IMPHTTAB reference files. The F280N filter did not require a change in scaling to match the count rates, so the revised solution is identical to the original.

**Table 4.** The chip sensitivity ratio (PHTRATIO=PHTFLAM2/PHTFLAM1) from the February 2016 (column 2) and November 2016 (column 3) IMPHTTAB reference files. CALWF3 uses this ratio to scale the UVIS2 science array to match UVIS1. Column 4 gives the mean count rate ratio for stepped WD's on the two chips calibrated with the February IMPHTTAB. Because of significant differences in the UV filter response, offsets in the mean count rate across chips are as large as 2%. Using a revised IMPHTTAB, column 5 shows that the count rate ratio is now  $\sim 1.0$  to within the statistical errors.

Filter	PHTRATIO Feb 2016 'zcv2057li_imp'	PHTRATIO Nov 2016 '0bi2206ti_imp'	Stepped WD (UVIS2 / UVIS1) 'zcv2057li_imp'	Stepped WD (UVIS2 / UVIS1) '0bi2206ti_imp'
F218W	0.779	0.774	1.010 +/-0.009	1.004 +/- 0.009
F225W	0.827	0.811	1.021 +/-0.006	1.001 +/-0.006
F275W	0.951	0.943	1.019 +/-0.008	1.010 +/-0.008
F280N	0.982	0.982	1.002 +/-0.008	1.002 +/-0.008

With the revised UV chip-sensitivity ratio, the magnitude offset for rotated Omega-Cen images in Figure 19 (right) is now  $\sim 0.0$  for blue stars in F225W and  $\sim 1\%$  in F275W. This is consistent with the results of the stepped WD photometry in Table 4. One possible explanation for the remaining F275W offset is that the zeropoint calibration program places subarrays primarily in the corners of the two chips (e.g. the top-left corner of amp A and the bottom-left corner of amp C). As discussed in Section 5, the photometry of stepped WD's in F275W is  $\sim 1\%$  higher than the mean when placing the source at the left edge of the detector and is likely due to errors in the flat field for this filter. Since the entire left edge is  $\sim 1\%$  high, however, this error should cancel out when computing the chip ratio.

An alternate explanation is that the zeropoint calibration program has fewer observations on chip 2 compared to chip 1 (12 versus 28 images, respectively in F275W). Deustua et al. (2016) give the rms scatter of the 3 WD's used to compute the zeropoints as 0.002 in UVIS1 and 0.006 in UVIS2, reflecting the spread in the observed to synthetic photometry. More observations in UVIS2 have been obtained in recent calibration programs, and including these may reduce the scatter in UVIS2 and possibly resolve the 1% discrepancy.

Because the UV zeropoints show significant color terms, we investigate whether the strength of the crosshatch (and therefore the flat field) may also be sensitive to the color of the stimulus. Monochromatic flats obtained during ground testing with the Xenon lamp at -82C may be used to test this. For the F225W and F275W filters, flats were obtained using an optical stimulus at wavelengths 310 nm, 530 nm, 750 nm, and 1250 nm. The ratio of pairs of flats at different wavelengths shows no evidence of any residual pattern. The pixel histogram of these ratio images is a Gaussian distribution and shows no broad tail of low values, as seen in the F336W temperature ratio in Figure 4. By contrast, the ratio of monochromatic flats at 290 nm obtained at the warmer -49C and at 310 nm at the nominal -82C shows the expected crosshatch temperature residual.

## VII. Summary

Flats for four UV filters were obtained at a warmer detector temperature to achieve higher count rates, and these require corrections to the spatial response to match the nominal in-flight temperature. Ground test data in F336W were obtained at both temperatures, allowing for a study of the effect on the flat field. We were able to model the -82C flat by applying a simple linear correction to the -49C flat, and this is extended to the UV filters. Photometry of WD standards stepped across crosshatch features in the flat field show that the same relation applies (e.g. the size of the flux residual correlates linearly with the value of the flat field at that pixel). An additional low-frequency correction further improves differential photometry of crowded Omega-Cen cluster observations and reduces the scatter for stepped WD observations.

The new chip-dependent calibration is intended to produce uniform count rate photometry across the two UVIS chips for hot WD stars. This enables users to produce more accurate drizzled data products when combining observations from different chips. Because of differences in the UV filter response for each chip, the sensitivity ratio in the February 2016 image photometry table does not fully equalize the count rate for blue sources, and the residual offset is as large as 2% in F225W. A revised image photometry table was delivered in November 2016 to correct this issue, and our tests show that differential photometry is now consistent to within 1%.

While drizzled images make a pretty picture, they cannot be used for precise photometry in the UV, because the same count rate has different fluxes on the two chips. Precise photometry requires knowledge of the original chip 1 or 2 location, because the chips have different bandpasses and different flux calibrations (zeropoints). Deustua et al (2017) describe this effect in more detail and provide a roadmap for ‘backing out’ the sensitivity ratio applied by CALWF3 and treating the two chips as independent detectors.

While the UV zeropoints have color terms of several percent, the flats do not. Examining the ratio of monochromatic flats obtained over a large range of wavelengths, no residual pattern with wavelength is found. In the coming year, the WFC3 team will quantify color terms in the zeropoints using synthetic photometry of sources of varying spectral type.

UV-bright stars are few and far between, so the traditional method of deriving an L-flat from dithered star cluster data is less effective in the UV than at longer wavelengths. Using the spatial scanning technique and UV-bright double star, scanned calibration data will be a good validation of the new flat fields, since many more detector pixels are sampled with higher signal-to-noise (e.g. 0.1% photometry). These supplemental data may prove useful in further refining the UV spatial response.

## Acknowledgements

The author is grateful to Ralph Bohlin for reviewing this ISR and for his valuable mentoring on HST photometry for nearly two decades. Susana Deustua is credited for her diligence in understanding the count rate offsets found in this study and for delivering a



revised sensitivity calibration which matches the UV count rate across the two chips. Varun Bajaj is acknowledged for his work creating and testing reference files for delivery and for his very helpful feedback in discussions about the chip dependent solutions. The author also thanks Harish Khandrika and Clare Shanahan for performing independent tests with supplementary calibration data to confirm the count rate offsets for blue sources when using the February 2016 chip sensitivity ratios.

## References

- Anderson, J., Bedin, L. R., Piotto, G., Yadav, R. S., & Bellini, A. 2006, *A&A*, 454, 1029
- Baggett, S. 2007, WFC3 ISR 2007-14, “WFC3 Ambient-2 Testing: Calibration Subsystem Performance”
- Bellini, A., Anderson, J., and Bedin, L.R. 2011, *PASP*, 123, 622B
- Brown, T. M. 2006, WFC3 ISR 2006-03, “Filter Throughputs for WFC3 SYNPHOT Support”
- Brown, T. M. 2008, WFC3 ISR 2008-48, “WFC3 TV3 Testing: System Throughput on the UVIS Build 1’ Detector”
- Deustua, S., Mack, J., & Bowers, A. S. 2016, WFC3 ISR 2016-03, “UVIS 2.0: Photometric Calibration”
- Deustua, S., Bohlin, R. C., Mack, J., & Bajaj, V. 2017, WFC3 ISR 2017-07, “WFC3 Chip Dependent Photometry with the UV filters”
- Giavalisco, M., et al. 2002 “Wide Field Camera 3 Instrument Mini-Handbook”, Version 1.0, (Baltimore: STScI)
- Gunning, H., Baggett, S. & MacKenty, J., 2014, WFC3 ISR 2014-18, “Pixel-to-Pixel Flat Field Changes in WFC3/UVIS”
- Mack, J., Sabbi, E., & Dahlen, T. 2013, WFC3 ISR 2013-10, “In-flight Corrections to the WFC3 UVIS Flat Fields”
- Mack, J., Rajan, A., & Bowers, A. S. 2015, WFC3 ISR 2015-18, “Spatial Accuracy of the UVIS Flat Fields”
- Mack, J., Dahlen, T., Sabbi, E., & Bowers, A. S. 2016, WFC3 ISR 2016-04, “UVIS 2.0: Chip-Dependent Flats”
- Sabbi, E. 2008, WFC3 ISR 2008-12, “UVIS CASTLE Photometric Filter Flat Field Atlas”
- Sabbi, E., Dulude, M., Martel, A.R., Baggett, S., & Bushouse, H. 2009, WFC3 ISR 2008-46, “WFC3 Ground P-flats”
- Strolger, L.-G. & Rose, S., eds. 2017 “HST Call for Proposals for Cycle 25”

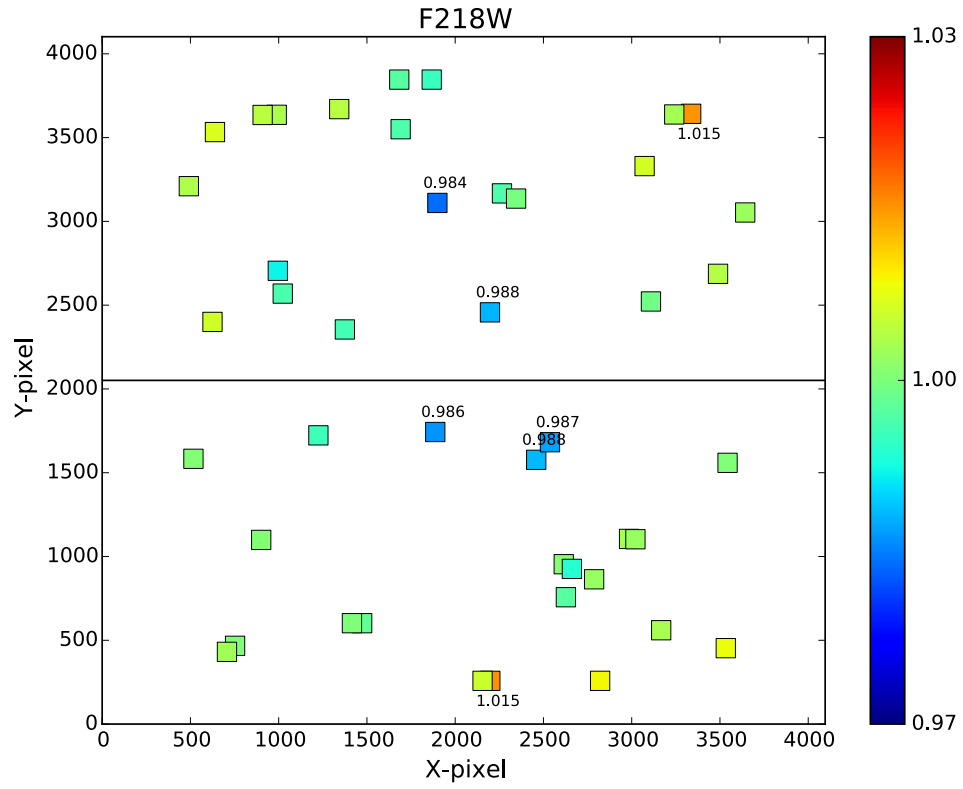
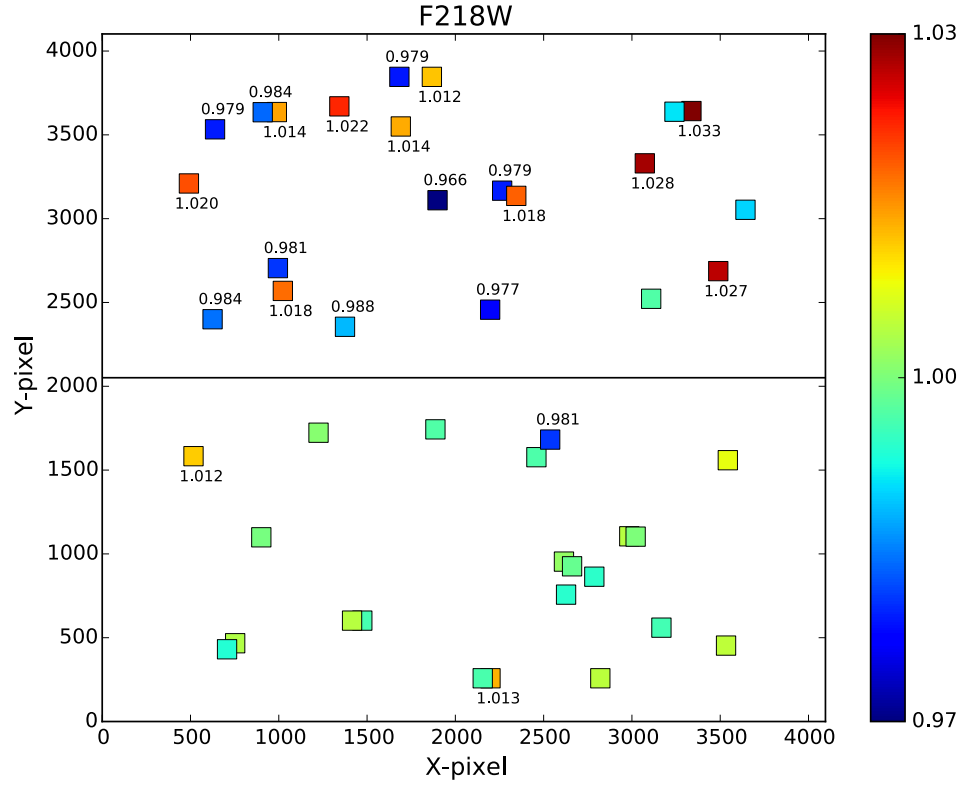


**Figure 21: F218W fractional residual relative to the mean flux per chip for G191B2B using the 2011 flats (top) and the 2016 flats (bottom).**

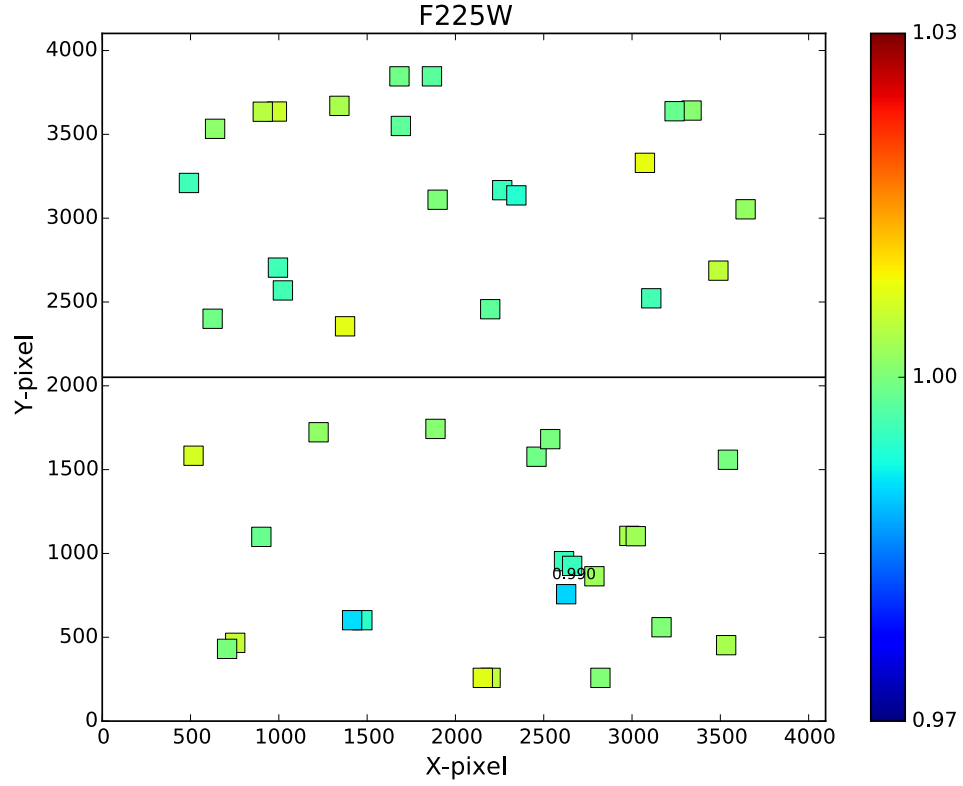
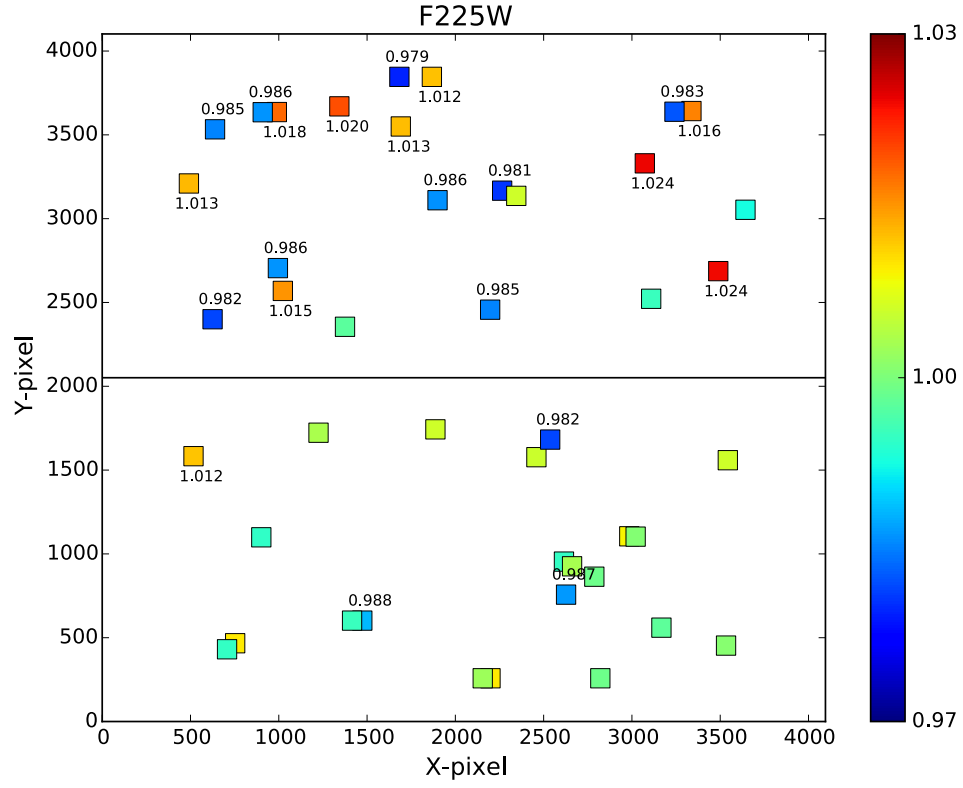


**Figure 22: F225W fractional residual relative to the mean flux per chip for GD71 using the 2011 flats (top) and the 2016 flats (bottom).**

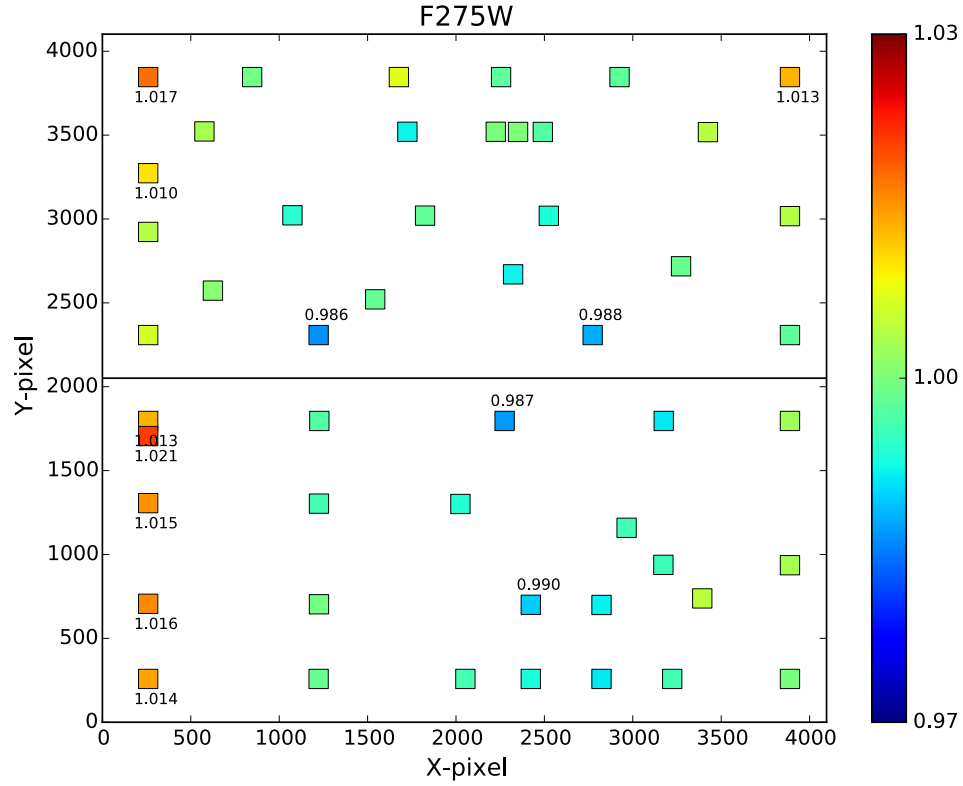
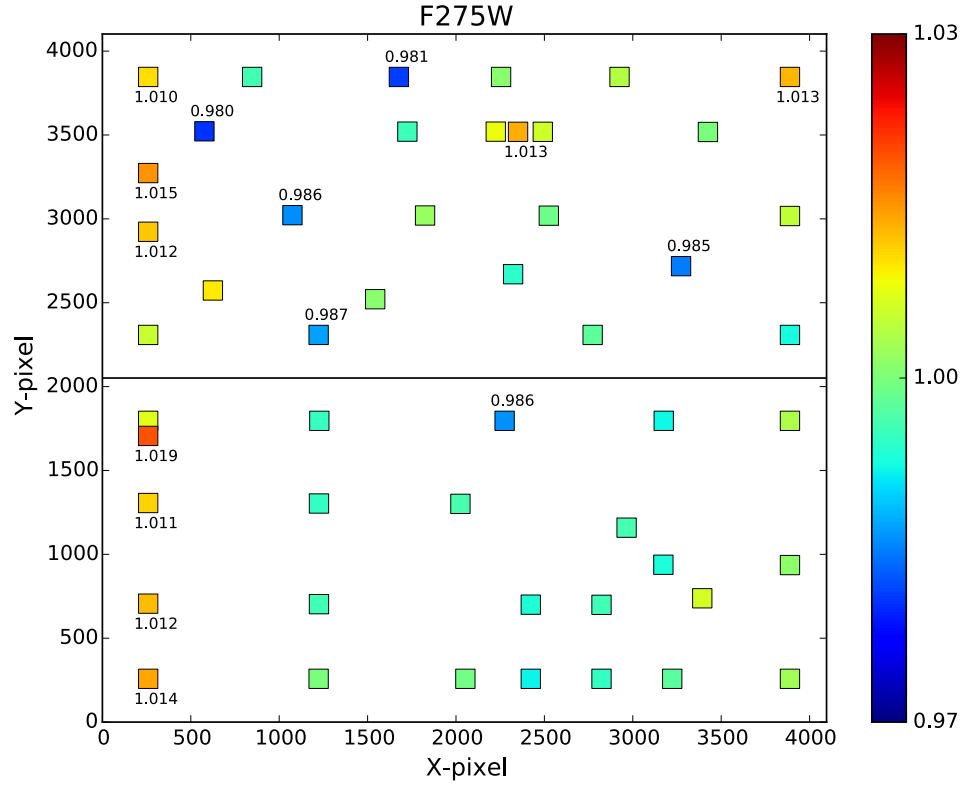


**Figure 23: F275W fractional residual relative to the mean flux per chip for G191B2B using the 2011 flats (top) and the 2016 flats (bottom).**

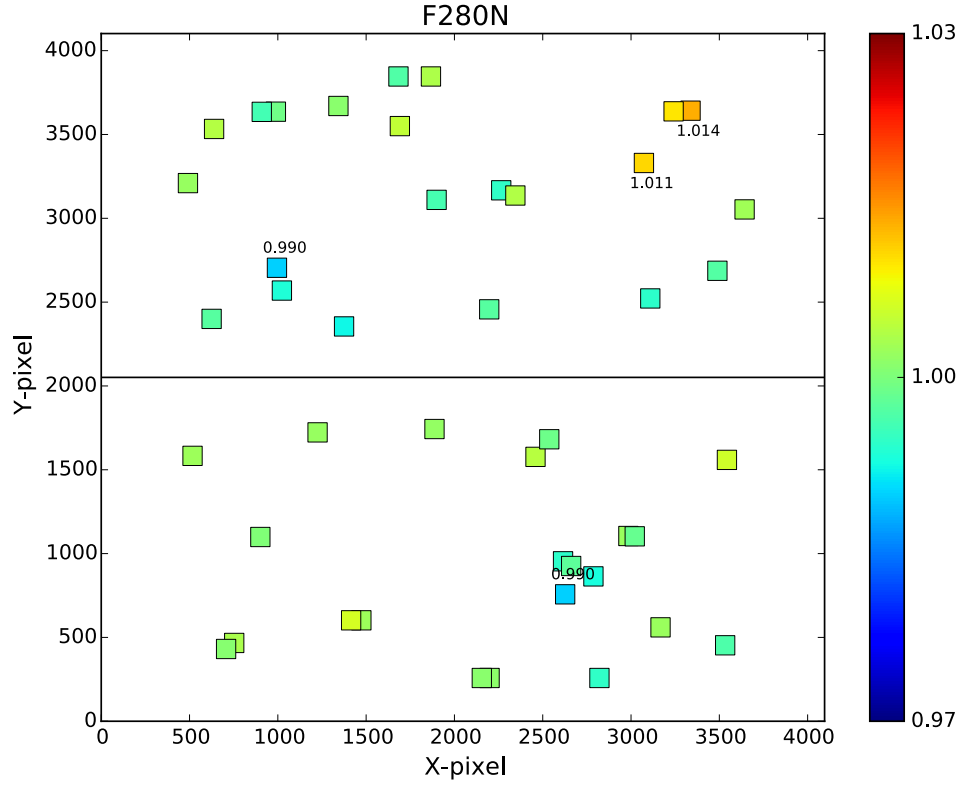
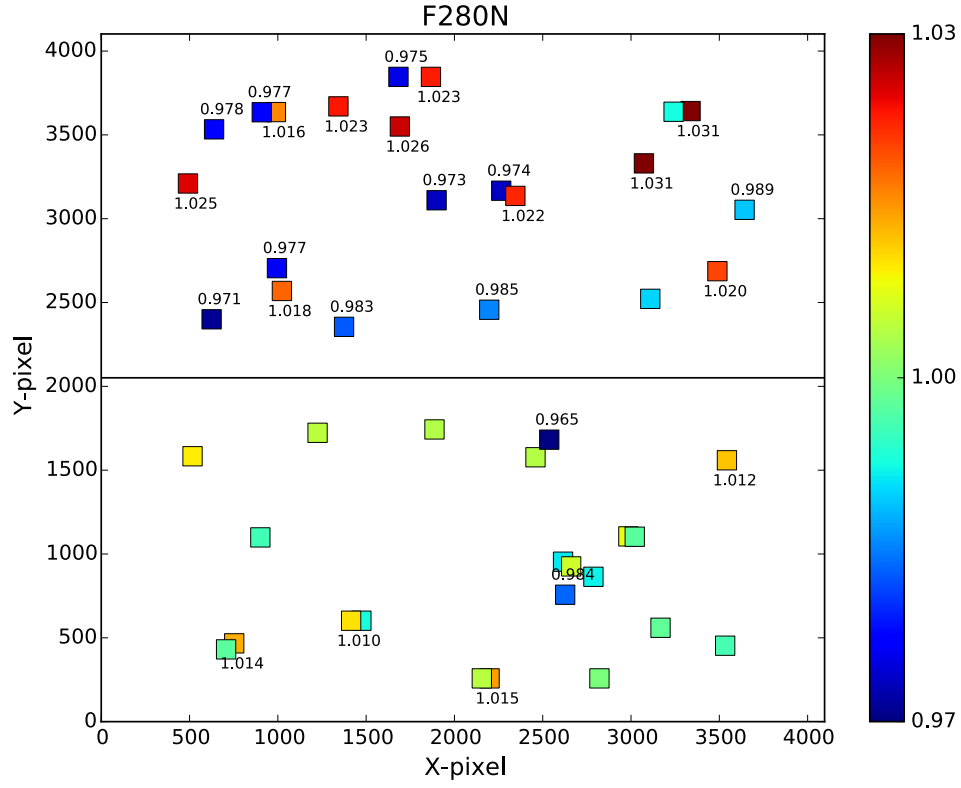


**Figure 24: F280N fractional residual relative to the mean flux per chip for BD+75D325 using the 2011 flats (top) and the 2016 flats (bottom).**